Conserved mechanisms of microtubule-stimulated ADP release, ATP binding, and force generation in transport kinesins

Joseph Atherton, Irene Farabella, I-Mei Yu, Steven S Rosenfeld, Anne Houdusse, Maya Topf, Carolyn A Moores

DOI: http://dx.doi.org/10.7554/eLife.03680

Cite as: eLife 2014;10.7554/eLife.03680

Received: 13 June 2014
Accepted: 8 September 2014
Published: 10 September 2014

Conserved mechanisms of microtubule-stimulated ADP release, ATP binding, and force generation in transport kinesins

Joseph Atherton[1], Irene Farabella[1], I-Mei Yu[2], Steven S. Rosenfeld[3], Anne Houdusse[2], Maya Topf[1], Carolyn A. Moores[1]*

[1] Institute of Structural and Molecular Biology, Birkbeck College, London, WC1E 7HX, UK
[2] Structural Motility, Institut Curie, Centre National de la Recherche Scientifique, Unité Mixte de Recherche 144, 75248 Paris Cedex 05, France
[3] Department of Cancer Biology, Lerner Research Institute, Cleveland Clinic, Cleveland, OH 44195, USA

** Corresponding author:*
Carolyn A. Moores
Institute of Structural and Molecular Biology,
Department of Biological Sciences,
Birkbeck College,
Malet Street,
London WC1E 7HX
UK
Tel: +44 207 631 6858
E-mail: c.moores@mail.cryst.bbk.ac.uk

Major subject area: Biophysics and structural biology

Abstract

Kinesins are a superfamily of microtubule-based ATP-powered motors, important for multiple, essential cellular functions. How microtubule binding stimulates their ATPase and controls force generation is not understood. To address this fundamental question, we visualized microtubule-bound kinesin-1 and kinesin-3 motor domains at multiple steps in their ATPase cycles – including their nucleotide-free states - at ~7Å resolution using cryo-electron microscopy. In both motors, microtubule binding promotes ordered conformations of conserved loops that stimulate ADP release, enhance microtubule affinity and prime the catalytic site for ATP binding. ATP binding causes only small shifts of these nucleotide-coordinating loops but induces large conformational changes elsewhere that allow force generation and neck linker docking towards the microtubule plus end. Family-specific differences across the kinesin-microtubule interface account for the distinctive properties of each motor. Our data thus provide evidence for a conserved ATP-driven mechanism for kinesins and reveal the critical mechanistic contribution of the microtubule interface.

INTRODUCTION

Kinesins are a large family of microtubule (MT)-based motors that play important roles in many cellular activities including mitosis, motility and intracellular transport (Hirokawa et al., 2010; Hirokawa and Noda, 2008; Vale, 2003). Their involvement in a range of pathological processes also highlights their significance as therapeutic targets and the importance of understanding the molecular basis of their function (Greber and Way, 2006; Henry et al., 2006; Liu et al., 2012b; Mandelkow and Mandelkow, 2002; Stokin and Goldstein, 2006). Kinesins are defined by their motor domains, which contain both the MT and ATP binding sites. Three ATP binding motifs - the P-loop, switch I, switch II - are highly conserved among kinesins (Sablin et al., 1996), myosin motors and small GTPases (Vale, 1996). Kinesins also share a conserved mode of MT binding (Alonso et al., 1998; Woehlke et al., 1997) such that MT binding, ATP binding and hydrolysis are functionally coupled for efficient MT-based work.

A number of kinesins drive long distance transport of cellular cargo (Hirokawa et al., 2010; Soppina et al., 2014), with dimerisation allowing them to take multiple 8nm ATP-driven steps towards MT plus ends (Svoboda et al., 1993). Their processivity depends on communication between the two motor domains, which is achieved via the neck linker that connects each motor domain to the dimer-forming coiled-coil (Clancy et al., 2011; Hackney, 1994; Rice et al., 1999; Tomishige and Vale, 2000). In the presence of MTs, ATP binding stimulates neck linker association (docking) with the motor domain towards the MT plus end, while ATP hydrolysis and MT release causes neck linker undocking (Asenjo et al., 2006; Rice et al., 1999; Skiniotis et al., 2003; Vale and Milligan, 2000); thus the neck linker is required for both intra-dimer communication and directionality. However, even when the role of the motor N-terminus in reinforcing neck linker movement via cover neck bundle (CNB) formation is considered (Hwang et al., 2008; Khalil et al., 2008), the contribution of neck linker docking to the force generating mechanism(s) of these kinesins remains uncertain (Rice et al., 2003; Rice et al., 1999; Vale and Milligan, 2000). New insights into the conformational rearrangements of these motors when bound to MTs are essential to reveal how they produce force.

The high resolution X-ray structures of a range of kinesin motor domains have established a major communication route from the nucleotide binding site via helix-α4 (the so-called relay helix) to the neck linker, such that alternate conformations of helix-α4 either block or enable neck linker docking (Kikkawa et al., 2001; Vale and Milligan, 2000). However, the neck linker conformation seen in these MT-free structures is not always correlated to the nucleotide

bound (Grant et al., 2007; Vale and Milligan, 2000). Cryo-electron microscopy (cryo-EM) has played a major role in elucidating several aspects of MT-bound kinesin mechanochemistry (Goulet et al., 2012; Goulet et al., 2014; Hirose et al., 2006; Kikkawa and Hirokawa, 2006; Rice et al., 1999; Sindelar and Downing, 2007, 2010; Skiniotis et al., 2003; Sosa et al., 1997; Sosa and Milligan, 1996). Despite these contributions, and despite recent advances in the study of kinesin-tubulin complexes using X-ray crystallography (Gigant et al., 2013), several outstanding questions concerning kinesin mechanochemistry remain. Specifically, the mechanism by which MT binding stimulates the kinesin ATPase and in particular enhances Mg-ADP release by several orders of magnitude is not clear (Hackney, 1988; Ma and Taylor, 1997; Sindelar, 2011). Although several speculative models have been proposed, an unambiguously interpretable structure of nucleotide-free MT-bound kinesin is currently lacking and is clearly critical in establishing how such transitions are achieved. Such a structure would also provide key insights into how ATP binding is coupled to both neck linker docking and force generation.

To address these major questions, we describe the MT-bound mechanochemical cycles of two plus-end directed human kinesin motor domains, a kinesin-1 (Kif5A) and a kinesin-3 (Kif1A) using cryo-EM structure determination at subnanometer resolution. Kinesin-1s (Kin1) and kinesin-3s (Kin3) are both important neuronal plus-end directed transport motors (Hirokawa et al., 2009b), but recent data suggest that Kin3 rather than Kin1 motors specifically are involved in long distance transport (Soppina et al., 2014). Their motor domains share 41% sequence identity, but profoundly different mechanochemistries – in which Kin1 dimers take processive steps and Kin3 monomers diffuse along MT tracks - have been proposed for these motors (Hirokawa et al., 2009a; Sindelar, 2011). Thus we wanted to investigate these differences and compare the motors side by side. The high quality of our reconstructions, coupled to flexible fitting, enables new insights into the kinesin mechanism. In particular, nucleotide-free reconstructions for both motor domains reveal a conserved mechanism whereby MT binding stimulates changes at the nucleotide-binding site favouring Mg-ADP release, and conformationally primes the motor to receive Mg-ATP. We also show that relatively small structural transitions occur at the nucleotide-binding site on Mg-ATP binding, but that these lead to larger scale conformational changes and neck linker docking. Structural analysis of two different transport kinesins allows a direct comparison of their conserved mechanochemical features and identification of attributes that confer distinctive properties on each motor.

RESULTS

MT-bound Kin1 and Kin3 reconstructions: an overview

We calculated MT-bound Kin3 reconstructions and pseudo-atomic models in four different nucleotide states: 1) Mg-ADP; 2) no nucleotide (NN), using apyrase treatment; 3) Mg-AMPPNP (a non-hydrolysable ATP analogue) and 4) Mg-ADPAlFx (an ATP hydrolysis transition state mimic), consistent with the previously described tight association of the Kin3 motor domain with MTs throughout its ATPase cycle (Table 1,2, Figure 1 - figure supplements 1,2; (Okada and Hirokawa, 2000). We also calculated three Kin1 reconstructions and pseudo-atomic models: 1) no nucleotide (NN), 2) Mg-AMPPNP and 3) Mg-ADPAlFx (Table 1,2, Figure 1 - figure supplements 1,2). Steady-state ATPase activities of the proteins that we used for our cryo-EM reconstructions (Table 3) show that the catalytic turnover of these motors are similar, but that the K_mMT of Kin3 is ~250x lower than Kin1. These values are broadly consistent with previous reports and also with our ability to form complexes for structure determination (Okada and Hirokawa, 1999; Sindelar and Downing, 2010; Woehlke et al., 1997). The conformations of both Kin3 and Kin1 in Mg-AMPPNP and Mg-ADPAlFx states were indistinguishable from each other at the resolution of our reconstructions (global RMSD: Kin3 ADPAlFx/AMPPNP= 0.7Å; Kin1 ADPAlFx/AMPPNP= 0.6Å), as had been previously shown in other studies of transport kinesins (Kif5B; (Gigant et al., 2013; Sindelar and Downing, 2010). Thus, for simplicity, we describe here one Mg-ATP-analogue ("Mg-ATP-like") reconstruction for each kinesin (Kin3: Mg-ADPAlFx; Kin1: Mg-AMPPNP). Views of the alternative Mg-ATP-like reconstructions for each kinesin are shown in figure supplements.

All our reconstructions have as their asymmetric unit a triangle-shaped motor domain bound to an $\alpha\beta$-tubulin dimer within the MT lattice (Figure 1). The structural comparisons below are made with respect to the MT surface, which, at the resolution of our structures (~7Å, Table 1), is the same (CCC>0.98 for all). As is well established across the superfamily, the major and largely invariant point of contact between kinesin motor domains and the MT is helix-α4, which lies at the tubulin intradimer interface (Figure 1C, Kikkawa et al., 2001). However, multiple conformational changes are seen throughout the rest of each domain in response to bound nucleotide (Figure 1D). Below, we describe the conformational changes in functionally important regions of each motor domain starting with the nucleotide-binding site, from which all other conformational changes emanate.

MT binding drives Mg-ADP release and primes the nucleotide-binding site to respond to Mg-ATP binding

The nucleotide-binding site (Figure 2) has three major elements: 1) the P-loop (brown) is visible in all our reconstructions; 2) loop9 (yellow, contains switch I) undergoes major conformational changes through the ATPase cycle, and 3) loop 11 (red, contains switch II) that connects strand-β7 to helix-α4, the conformation and flexibility of which is determined by MT binding and motor nucleotide state. The presence or absence of density for nucleotide in the nucleotide-binding site in each reconstruction (Figure 2 and Figure 2 – figure supplement 5) is consistent with the well-established sample preparation methods used (see Materials and Methods). In the Kin3-Mg-ADP reconstruction, the N-terminal half of helix-α4 lies at the back of the nucleotide-binding site where its N-terminal end is partially flexible (Figure 2A). ~50% of the adjacent loop11 is not visible presumably also due to flexibility, and density for this loop is only visible close to the P-loop at the edge of the motor's central β-sheet. In contrast, density corresponding to loop9 is clearly defined: the 4-turn helix-α3 is broken by a single residue, before two further helical segments are seen, one of which coordinates Mg-ADP, together with switch II (Coureux et al., 2003; Hirose et al., 2006; Kull and Endow, 2013). The conformations of loop9 and loop11 in this reconstruction are thus essentially the same as is seen in the Kin3-Mg-ADP crystal structure (Kikkawa et al., 2001).

In the Kin3-NN reconstruction (Figure 2B), the N-terminus of helix-α4 is fully stabilised, while the C-terminal portion of loop11 adopts a helical turn that forms a new contact with α-tubulin that likely contributes to the strengthened motor domain-MT interaction in the NN state (Nakata et al, 1995). Density corresponding to the rest of loop11 is now also fully visible, such that switch II is seen running from the β-sheet core past the P-loop. Loop9 has undergone a large conformational change: helix-α3 now terminates after four turns and the resulting elongated conformation of loop9 forms a finger-like extension that reaches towards the nucleotide pocket and the new helical turn in loop11. Density connects this extended form of loop9 and the N-terminus of helix-α4; density also connects the P-loop and loop9 (as previously described for Kif5B; Sindelar, 2011; Sindelar and Downing, 2007). The Kin1-NN reconstruction shows a very similar configuration at the nucleotide-binding site (Figure 2D). This arrangement of the nucleotide binding loops in both motors is striking because even in the absence of bound nucleotide, the loops adopt a conformation related (but not identical) to that formed when Mg-ATP is bound (Chang et al., 2013; Gigant et al., 2013; Parke et al., 2010). That is, MT-stimulated Mg-ADP release appears to conformationally prime the switch loops for Mg-ATP binding. The similarity of these reconstructions supports the idea of a conserved mechanism of 1) MT-induced Mg-ADP release (Figure 2

– figure supplement 3) and 2) MT priming of the conformation of the nucleotide-binding pocket to receive Mg-ATP in both Kin1s and Kin3s.

Because of this conformational priming, structural changes in the nucleotide-binding site upon ATP binding are comparatively small when the NN and Mg-ATP-reconstructions are compared (Figure 2B-E, Figure 2 – figure supplement 1). In both Kin3 and Kin1, loop9 now reaches further into the nucleotide-binding pocket to cradle the Mg-ATP mimic, enclosing it in a catalytically competent conformation and forming continuous density with the nucleotide and P-loop (Figure 2C,E). The C-terminus of loop11 retains a helical turn conformation similar to that observed in the nucleotide free reconstructions. Density for the N-terminus of loop11 runs from the core β-sheet past the P-loop and the γ-phosphate mimic. Importantly however, in comparison to the nucleotide-free reconstruction, the loop11 helical turn shows reduced contact with tubulin and has moved toward loop9 and helix-α□ (see arrow, Figure 2C,E). The 'pincer-like' movement of the switch loops is associated with formation of a prominent connection of density between them and is consistent with a 'phosphate tube' structure similar to that described recently for other kinesins (Chang et al., 2013; Gigant et al., 2013; Parke et al., 2010; Sindelar and Downing, 2010). We note that, although the structure of the mammalian Kin1 Kif5A bound to MT has not previously been determined, our Kif5A reconstruction displays the major features seen in the recently published tubulin dimer-bound Kif5B Mg-ADPAlFx X-ray structure and to previous Mg-ATP analogue Kif5B cryo-EM reconstructions (Gigant et al., 2013; Sindelar and Downing, 2007, 2010). Overall, in response to the presence of γ-phosphate, loop9 and loop11 draw closer to each other and to helix-α6 in both motors. This movement also reduces the density that connects loop11 with the MT.

Movement and extension of helix-α6 controls neck linker docking

As shown in Figure 2, the N-terminus of helix-α6 is closely associated with elements of the nucleotide-binding site suggesting that its conformation alters in response to different nucleotide states. In addition, because the orientation of helix-α6 with respect to helix-α4 controls neck linker docking (Kikkawa et al., 2001; Vale and Milligan, 2000), and because helix-α4 is held against the MT during the ATPase cycle, conformational changes in helix-α6 control movement of the neck linker.

In the Kin3-Mg-ADP reconstruction, helix-α6 contacts α-tubulin as was previously reported (Figure 3A, arrowhead; Kikkawa and Hirokawa, 2006); this interaction is likely to involve basic residues conserved in Kin3 (see alignment in Figure 6A) and negatively charged residues in the N-terminal

region of α-tubulin H12. The small β-sheet composed of strands-β1a,b,c (β-sheet1$_{abc)}$ lies on top of helix-α6 and above the MT surface; this β-sheet is situated roughly perpendicular to the core β-sheet of the motor domain, and contains the characteristically extended Kin3 loop2. In the Kin3-Mg-ADP state, the orientation of helix-α6 with respect to helix-α4 ensures both that helix-α6 cannot fully extend and the neck linker is undocked; this is indicated, first, by a lack of density between helix-α4 and helix-α6, and second by a lack of density along the core β-sheet (Figure 3 - figure supplement 3A). The neck-linker is mainly invisible and presumably disordered, consistent with previous reports (Rice et al, 1999; Skiniotis et al, 2003). However, some density that probably corresponds to the N-terminus of the neck linker is visible extending from the C-terminus of helix-α6, suggesting its flexible conformations are directed largely towards the MT minus end (Figure 3A, arrow and Figure 3 - Figure supplement 3A). Density that is likely to correspond to the Kin3 N-terminus is also visible, but no single conformation can be distinguished.

In the Kin3-NN reconstruction, contact between helix-α6 and α-tubulin remains fixed, although the C-terminal end of helix-α4 is disconnected from the MT at its junction with the helix-α6 C-terminus (Figure 3B). The relative orientation of these helices ensures that the neck linker remains undocked and flexible; this is again indicated by the gap separating these helices and by density extending from the C-terminus of helix-α6, similar to that described in the Mg-ADP state (Figure 3B and Fig 3 - figure supplement 3B). The flexible distribution of the N-terminus is also unaltered. The Kin1-NN reconstruction shows an overall similar configuration in the region of helix-α6, with its neck linker undocked and flexible and its N-terminus disordered (Figure 3D and Fig 3 - figure supplement 3E). However, some family specific differences are apparent, both within the motor domain structure and at the motor-MT interface (Figure 3D). For example, in Kin1 β-sheet1$_{abc}$ appears more compact than in Kin3 because loop2 and loop3 are shorter. In Kin1 helix-α6, differences are present in the charged residues compared to Kin3 (see Figure 6A, described in more detail below) and, perhaps as a consequence, the C-terminus of Kin1 helix-α6 is connected by less density to the MT surface compared to Kin3 (Figure 3B,D, arrowhead). Thus, relatively limited conformational changes appear to accompany Mg-ADP release in the vicinity of helix-α6 and the neck linker. This is despite the previously described significant rearrangement of the switch loops at the nucleotide-binding site on the other side of the domain (Figure 2).

However on Mg-ATP binding, a major conformational change of helix-α6 is observed in both motors (Figure 3C,E; Figure 3 – figure supplement 1). Compared to the NN reconstructions, helix-α6 and β-sheet1$_{abc}$ have together

lifted and rotated away from the MT surface. In the Mg-ATP-like reconstructions, a hydrophobic cavity forms above helix-α4 (Kikkawa et al., 2001) because the central β-sheet has peeled away from its C-terminal end (see Figure 3C,E; and Figure 3 – figure supplements 2 and 3C,D,F,G) helix-α6's C-terminus extends by a turn and inserts into this cavity. In the Kin3-Mg-ATP-like reconstruction, as a result of the repositioning of helix-α6, only a narrow bridge of density connects its N-terminal end with α̃□□□□□□□ (Figure 3C, arrowhead). This N-terminal end is more negatively charged than the C-terminal end of helix-α6 that was in contact with the MT surface prior to Mg-ATP binding. In Kin1, density for helix-α6 disconnects from the MT surface altogether (Figure 3E, arrowhead). Importantly, in both motors, this structural reorganisation allows the neck linker to extend towards the MT plus end and dock along strand-β8 of the central β-sheet (Figure 3C,E and Figure 3 - figure supplement 3C,D,F,G) (Rice et al., 1999). The N-termini of both motors are also directed towards the MT plus end, lying across the docked neck linker to form the CNB (Figure 3 - figure supplement 3C,D,F,G and Figure 4C,E) (Hwang et al., 2008; Khalil et al., 2008). Thus, concerted conformational changes involving a number of structural elements appear to contribute to movement of helix-α6 and neck linker docking.

A stable motor domain-MT interface is maintained through the ATPase cycle

These analyses show that in both Kin1 and Kin3, the same, small conformational changes at the nucleotide binding site on Mg-ATP binding have large structural consequences elsewhere. One important aspect of transmission of this mechanochemical information is that a stable interaction with the MT is sustained. Our data show that several structural elements form apparently invariant contacts with the MT (primarily β-tubulin) in all the nucleotide states we examined. In the Kin3 reconstructions, density corresponding to helix-α4 runs across the whole motor domain-MT interface (Figure 4A-C). At its C-terminal end, density corresponding to the N-terminal portion of the extended Kin3 loop12 sequence is stabilised as a helical turn (Figure 4A-C, pink). However, density corresponding to the middle, Kin3-characteristic Lys-rich portion of this loop (the so-called K-loop) is not visible in any nucleotide state (Figure 4A-C, pink dotted line). This suggests that this highly basic middle section of loop12 remains mobile even while close to the MT surface (discussed below). The C-terminal end of Kin3 loop12, on the other hand, is visible and is stabilised by interaction with β-tubulin. Loop12 leads into an interconnected region of contacts between the MT surface and the motor, composed of helix-α5 along with loop8/strand-β5. These elements do not alter their interaction with the MT in the different nucleotide states calculated (Figure 4A-C; Figure 4 – figure supplement 1).

The Kin1 reconstructions show the same structural components at the motor domain-MT interface, which are also invariant in the different nucleotide states (Figure 4D,E). In the Kin1 reconstructions - as with Kin3 - helix-α4 forms a major contact at the tubulin intradimer interface, and adopts a conserved orientation relative to the MT (Figure 4D,E). However, the C-terminus of the Kin1 helix-α4 is shorter by one turn compared to Kin3 because its loop12 is shorter and also lacks the lysine cluster characteristic of Kin3s (compare e.g. Figure 4B and D). Density corresponding to the Kin1 loop12 connects directly to helix-α5 at the MT interface (Figure 4D,E; Figure 4 – figure supplement 1). However, in contrast to Kin3, there is no density in our reconstructions connecting Kin1 loop8/strand-β5 and the MT surface (Figure 4D,E).

Mechanical amplification and force generation involves conformational changes across the motor domain

A key conformational change in the motor domain following Mg-ATP binding is peeling of the central β-sheet from the C-terminus of helix-α4 increasing their separation (Figure 3- figure supplement 2); this is required to accommodate rotation of helix-α6 and consequent neck linker docking (Figure 3 B-E). Peeling of the central β-sheet has previously been proposed to arise from tilting of the entire motor domain relative to static MT contacts, pivoting around helix-α□ (the so-called 'seesaw' model; Sindelar, 2011). Specifically, this model predicts that the major difference in the motor before and after Mg-ATP binding would be the orientation of the motor domain with respect to helix-α4 (Vale and Milligan, 2000). Globally, the conformations of both Kin1 and Kin3 in our reconstructions are consistent with motor domain tilting of 12-15º on Mg-ATP binding (Figure 3B-E, Figure 3 – figure supplement 2). In both motors, subtle flexure of the central β-sheet itself is also apparent on Mg-ATP binding (Figure 5 – figure supplement 1) such that loop7 and the bottom of strand-β3 that connects to the P-loop are not superimposable. Differences in the β-sheet when comparing the Kin3-Mg-ADP and Kin3-NN models are even smaller in comparison (Figure 5 – figure supplement 1A). In myosin, the equivalent structural region undergoes substantial β-sheet flexure on nucleotide release (backbone RMSD >3.2Å, Figure 5 – figure supplement 1D; (Coureux et al., 2003; Reubold et al., 2003). However, our data provide no evidence of significant flexing in the kinesin β-sheet that has been proposed to accompany Mg-ADP release (Kull and Endow, 2013). Furthermore, although the slight β-sheet bending that occurs when Mg-ATP binds may contribute to force generation as previously suggested (Gigant et al., 2013), it cannot, by itself, account for the peeling of the β-sheet that allows neck linker docking.

If motor domain tilt were sufficient to account for the mechanochemical transmission that takes place on Mg-ATP binding, superposition of the β-sheets of the NN and Mg-ATP structural states would be predicted to bring the motor domains into alignment (apart from helix-α4 and the nucleotide-invariant MT contacts). However, such a superposition shows large residual differences in multiple regions of the motor domain (Figure 5A,B; depicted as RMSDs between each pair of NN/Mg-ATP models). This clearly demonstrates that the β-sheet tilting that occurs in the transition from NN to Mg-ATP is not sufficient to describe the conformational changes in either Kin3 or Kin1. This is further emphasized when the Kin3 and Kin1 NN pseudo-atomic models are superimposed on the β-sheets of their respective ATP-like docked models and compared to the Mg-ATP-like cryo-EM reconstructions (Figure 5C,D). Various parts of the NN models protrude from the density for the ATP-like reconstructions illustrating the poor fit, agreeing with the RMSD calculations and further supporting their tilt-independent movements (Figure 5C,D compare to Figure 2C,E). At the nucleotide-binding site, this analysis highlights that movement of loop9 around the bound Mg-ATP is large compared to motor domain tilting. Similarly, while loop11 retains a similar conformation before and after Mg-ATP binding, it does not tilt along with the core β-sheet but instead moves towards the motor domain core (see Figure 5 – figure supplement 2). In addition, helix-α2a and loop5 above the nucleotide-binding site, and helix-α0 below the nucleotide-binding site, accommodate Mg-ATP binding in both motors (Figure 5A,B). Some structural changes are seen in helix-α1, whereas the β-sheet1_{abc} shows clear conformational differences; family-specific loop insertions in loop2 and loop3 particularly exaggerate these movements in Kin3 (Figure 5C). The expected extension of helix-α6 and neck-linker docking is also highlighted by this analysis. However, it is also apparent that helix-α6 movement cannot be described purely by motor domain tilt, because it also undergoes a translational shift towards the MT plus end, as was recently proposed for Kin1 (Gigant et al., 2013). The improved resolution of our reconstructions thus allows us to conclude that the conformational changes that underlie force generation in both Kin1 and Kin3 involve: 1) motor domain tilting relative to static MT contacts, but also 2) more complex sets of movements that accommodate Mg-ATP binding and bring about mechanical amplification.

Differences in the Kin1/Kin3 MT interface provide structural insight into superprocessivity of Kin3s

Despite high structural and mechanistic similarity between Kin3 and Kin1, contacts across the motor domain-MT interface are likely to contribute to differences in these motors' transport properties (Figure 6). One major difference is the presence of a Lys-rich insertion in Kin3 loop12 (the 'K-loop')

(Fig6A, pink shading) (Okada and Hirokawa, 1999). In Kin3s, loop12 mediates 1D diffusion of ADP-bound monomeric and dimeric Kin3s along MTs via flexible, electrostatic interactions with the acidic C-terminal tails (CTTs) of tubulin (Kikkawa et al., 2000; Okada and Hirokawa, 1999, 2000; Soppina et al., 2014). The K-loop also enhances the initial interaction between Kin3 dimers and their track prior to processive stepping (Soppina & Verhey, 2014). In addition, whereas the catalytic turnover of Kin3 compared to Kin1 monomers are similar (our data in Table 3 and e.g. (Okada and Hirokawa, 2000), steady state ATPase assays show that the K_mMT of Kin3 is several hundred times lower than Kin1, a difference that depends partly on the K-loop (Okada & Hirokawa, 2000). Since the K_mMT is indicative of the MT affinity of ADP-bound kinesin (Woehlke et al, 1997), this is consistent with the role of the Kin3 loop12 in enhancing the association of Mg-ADP Kin3s with MTs (Kikkawa et al., 2000; Okada and Hirokawa, 1999, 2000; Soppina and Verhey, 2014).

There is no density corresponding to the K-loop - nor of the tubulin CTTs with which it is proposed to interact - in any of our Kin3 reconstructions (Fig4A-C). Given that density corresponding to Kin1 loop12 (Fig4D,E), and Kin3 loops of equivalent size (e.g. loops 2 and 3 (7 and 8 residues respectively), Fig3A-C) are clearly visualised, this suggests that this region of Kin3 is structurally heterogeneous and therefore invisible in the context of our averaging methods. The K-loop may be intrinsically flexible due to its sequence, consistent with its role in mediating 1D diffusion. In addition, the lack of structural detail in this region could be due to the biochemical heterogeneity (different isoforms and post-translational modifications) of the CTTs of the bovine tubulin used in our experiments. Our structures imply that conformational flexibility of the K-loop persists throughout the motor's ATPase cycle but more information from future experiments is needed to clarify the contribution of this region to motor function.

However, the K-loop is reported to account for only a 10-fold enhancement of MT association of monomeric Kin3s over Kin1s (Okada and Hirokawa, 1999, 2000), implying that other regions of the Kin3 motor domain also contribute. Our data show clear structural differences between Kin1 and Kin3 at the interface of the acidic tip of α-tubulin H12 with helix-α6, especially in the Mg-ADP/NN reconstructions (Figure 3). In addition, more subtle differences in the distribution of charged residues in loop11 and helix α4's N-terminus would be predicted to influence MT affinity (Figure 6D). Sequence divergence in loop8/strand-β5 was previously proposed to enable discrimination of post-translational modification in α-tubulin CTTs by Kin3 compared to Kin1 (Konishi and Setou, 2009). A direct role for recognition of the α-tubulin CTT is unlikely given its distance from loop8/strand-β5. However, differences in

connectivity between this region of the motor domain and β-tubulin when comparing Kin1 and Kin3 (Figure 4) could contribute to differences in their apparent overall affinity. Intriguingly, recent data show that the K-loop does not contribute to the super-processive stepping properties of Kin3 dimers (Soppina and Verhey, 2014). Although a number of motor parameters could in principle contribute to processivity (e.g. coordination between dimer motor domains via the NL (Clancy et al, 2011), our structures suggest that other regions of the Kin3-MT interface may also influence functional differentiation of these motors including super-processivity (Figure 6C,D).

DISCUSSION

Kinesin mechanochemistry and the extent of mechanistic conservation within the motor superfamily are open questions, critical to explain how MT binding, and ATP binding and hydrolysis drive motor activity. Our structural characterisation of two transport motors now allows us to propose a model that describes the roles of mechanochemical elements that together drive conserved MT-based motor function (Figure 7).

In the Mg-ADP-bound kinesin, association with the MT surface is experienced directly by loop11 and the N-terminus of helix-α4, biasing their conformations towards more structured states. Full stabilisation of these elements is not achieved until Mg-ADP is released, and the additional contacts with the MT surface may in particular serve to nucleate the single turn helix in loop11. This is consistent with the well-documented role of loop11 in sensing MT attachment and triggering Mg-ADP release via interactions with α-tubulin (Ebbing et al., 2008; Uchimura et al., 2010; Woehlke et al., 1997; Yun et al., 2001). Loop9 does not directly contact the MT before or after Mg-ADP release, but dramatically changes conformation, unfurling and extending around the nucleotide-binding site. The structured conformations of loop11 and the N-terminus of helix-α4 are sterically compatible with the conformations of loop9 before and after Mg-ADP release – i.e. no clashes are seen in either case. However, the extended conformation of loop9 and the ordered conformations of helix-α4/loop11 are likely to be mutually stabilising due to formation of additional contacts, and thereby mediate communication between the nucleotide and MT-binding sites (Ebbing et al., 2008; Farrell et al., 2002; Nitta et al., 2008; Woehlke et al., 1997; Yun et al., 2001). Critically, however, the water network coordinating Mg-ADP is stabilized exclusively by the retracted helical conformation of loop9 (Figure 2 – figure supplement 2). The transition towards the extended conformation of loop9 promotes Mg-ADP release by destabilisation of Mg coordination (Nitta et al., 2008). These structural rearrangements therefore indicate that sequential conformational changes of the switch loops in the presence of MTs stimulate Mg-ADP release, the rate-limiting step of motors in solution (Hackney, 1988). These rearrangements allow formation of a nucleotide-free motor that is strongly bound to its MT track (Nakata and Hirokawa, 1995), at least in part due to additional contacts formed between loop11 and the MT.

Conformational changes at the nucleotide-binding site that lead to Mg-ADP release also appear to prime the kinesin motor domain for Mg-ATP binding. However, the primed conformation clearly does not lead to neck linker docking in the absence of Mg-ATP, contrary to previous predictions (Nitta et al., 2008). Multiple strands of evidence suggest that the neck linkers of

transport kinesins in solution explore both docked and undocked conformations independent of the nucleotide state (Nitta et al., 2008; Rice et al., 1999; Scarabelli and Grant, 2013). Thus, tight MT binding is critical in strongly biasing neck linker conformation in the absence of nucleotide such that it will be undocked and, in our reconstructions, directed albeit flexibly towards the MT minus end. Interaction of helix-α6 with α-tubulin's H12 (Uchimura et al., 2010) may therefore help to prevent neck linker docking in the absence of nucleotide, despite changes in the conformations of the switch loops at the active site.

Mg-ATP binding does not cause large rearrangements of the nucleotide-binding site of MT-bound motor domains. However, the presence of the pre-hydrolysis γ-phosphate of Mg-ATP is critical for the pincer-like movement of loop11 and loop9 towards each other. Along with formation of strong additional contacts between these loops, the helix-α4 N-terminus and the P-loop (see Figure 2 - figure supplement 4 and Chang et al., 2013; Gigant et al., 2013; Parke et al., 2010), this new local connectivity induces the larger rearrangements that cause neck linker docking. The resulting conformational changes cannot be described only as a tilt of the motor domain relative to static contacts with the MT including helix-α4: in addition to β-sheet tilting, multiple changes across the domain reinforce mechanical amplification and neck linker docking when Mg-ATP binds. The resolution of our reconstructions also allows us to detect subtle distortion of the central β-sheet edges on Mg-ATP binding. However, arguably the most important consequences of Mg-ATP binding are the changes – extension, tilting and translation - in helix-α6 that allow neck linker docking. This conformation is stabilised by contacts between its N-terminus and elements in the nucleotide-binding pocket (see Figure 2 - figure supplement 4 and Chang et al., 2013; Gigant et al., 2013; Parke et al., 2010).

Neck linker docking is essential for both defining the directionality of kinesin motility and mediating head-head tension to ensure processive dimer stepping (Clancy et al., 2011; Rice et al., 1999; Sindelar, 2011; Skiniotis et al., 2003; Tomishige and Vale, 2000; Vale and Milligan, 2000), but whether docking itself can generate the force required for kinesin stepping has been questioned (Rice et al., 2003). Thus, the structural basis of ATP-dependent force generation remains a matter of debate in the field (Cross and McAinsh, 2014; Visscher et al., 1999). The conformational changes associated with helix-α6 during the ATPase cycle – in which contacts with the MT formed in the ADP/NN state are broken as Mg-ATP-dependent rotation pulls it away from the MT surface – reinforce neck linker movements, and may also contribute to mechanical amplification and force generation. The translation/extension of helix-α6 into the hydrophobic cavity that is created by

β-sheet tilting when Mg-ATP binds may ensure that this tilting is not reversed. Intriguingly, mutagenesis of residues at the helix-α6/neck linker junction has a profound effect on the activity of kinesin monomers (Case et al., 2000), pointing to the importance and likely conservation of structural transitions in this region (Case et al., 1997). Importantly, movement of helix-α6 also relieves steric blocking of neck linker docking and presumably biases the mobile neck linker trajectory. In collaboration with the motor N-terminus, formation of the CNB reinforces the plus end directionality of this bias. Thus we propose that the helix-α6 is a key mechanical element within the kinesin motor domain, and that its Mg-ATP-dependent movement is essential to plus-end directed stepping.

Once the neck linker has docked ATP hydrolysis occurs, ensuring efficient coupling between kinesin stepping, Mg-ATP binding and hydrolysis (Hahlen et al., 2006; Schnitzer et al., 2000). A detailed reaction mechanism for hydrolysis has been proposed based on the conformations of loop9 and loop11 (a so-called 'phosphate tube') with Mg-ATP-analogue bound (Parke et al., 2010). Consistent with MT binding being important in the catalytic enhancement of kinesins (Ma and Taylor, 1997), this hydrolysis competent configuration of the switch loops is rarely seen in Mg-ATP-analogue kinesin structures in the absence of MTs (e.g. Cochran et al., 2009; Kikkawa et al., 2001; Nitta et al., 2004, with Chang et al., 2013; Parke et al., 2010 being the notable exceptions); those in complex with tubulin always adopt this configuration (Gigant et al., 2013; Goulet et al., 2012; Sindelar and Downing, 2010). On Mg-ADP release, loop9 and loop11 are stabilized into conformations quite close to catalytically competent ones. This suggests that the conformational changes triggered by MT binding that lead to MT-stimulated ADP release also contribute to setting up the catalytic site for ATP hydrolysis. Thus, a subset of mutations in MT-sensing residues in loop11, or which decouple MT affinity and ADP-release also affect MT-stimulated ATP-hydrolysis (Ebbing et al., 2008; Song and Endow, 1998; Uchimura et al., 2010; Woehlke et al., 1997; Yun et al., 2001). Following hydrolysis and phosphate release, we would predict that the Mg-ADP remaining in the catalytic site causes retraction of loop9, subsequent destabilization of loop11 and the helix-α4 N-terminus, leading to track detachment.

This model allows several previously proposed hypotheses, in particular concerning MT-stimulated Mg-ADP release, to be excluded. Mechanisms that involve MT-induced 'opening' of the nucleotide pocket, disordering of the switch loops around the nucleotide pocket to destabilise Mg-ADP coordination, or in which loop9 extends into the nucleotide pocket to perturb the P-loop and eject Mg-ADP (Kikkawa and Hirokawa, 2006; Nitta et al., 2008; Sindelar, 2011; Sindelar and Downing, 2007; Yun et al., 2001) are not

supported by our observations that: 1) both loop9 and loop11 move towards the nucleotide-binding pocket on Mg-ADP release, 2) these loops adopt well-defined and conserved conformations that are clearly visualised after Mg-ADP release and, 3) the conformation of these loops does not sterically interfere with nucleotide binding or disrupt the P-loop. Another prominent idea is that a significant twist of the core β-sheet caused by MT attachment would promote Mg-ADP release analogous to the equivalent release step in myosin (Coureux et al., 2003; Hirose et al., 2006; Kull and Endow, 2013). However, comparison of our Kin3-Mg-ADP and Kin3-NN reconstructions (Figure 5 – figure supplement 1A) does not support β-sheet twist as a mechanism for Mg-ADP release in kinesins.

The structural elements involved in these mechanochemical transitions are extremely well conserved amongst kinesins, and it is likely that the mechanisms we describe are utilised by all superfamily members. We previously characterised the MT-bound ATPase cycle of human kinesin-5 (Kin5, Goulet et al., 2012; Goulet et al., 2014). Although the resolutions of those cryo-EM reconstructions (~10Å) do not provide the level of detail of the current work, many of our current hypotheses are consistent with a conserved mechanochemistry, specifically conformational coupling of loops9 and 11 to bring about MT-induced Mg-ADP release and Mg-ATP induced neck linker docking. Superimposed on this conserved mechanochemistry, family-specific modifications were also detected; most strikingly for Kin5, these include the proposed role of the Kin5 extended loop5 in controlling nucleotide binding, and the stiffer properties of the Kin5 neck linker that undergoes an order-to-order transition on Mg-ATP binding. Family-specific insertions elsewhere in the motor domain are likely to have other modifying roles, such as Kin3's loop12, which enhances the initial interaction between these highly processive motors and their tracks (Soppina and Verhey, 2014). A tantalising hint of how insertions in loop2 may be coupled to MT depolymerisation in for example kinesin-13s (Asenjo et al., 2013; Desai et al., 1999; Moores et al., 2002) and kinesin-8s (Peters et al., 2010; Varga et al., 2006) is provided by its proximity to the MT surface and the mechanical amplifier helix-α6, and by its large displacement on Mg-ATP binding. Future studies at high resolution will provide further insights into the ways this conserved mechanochemistry is modified in diverse functional contexts within the kinesin superfamily.

Materials and Methods

Protein purification

A human kinesin-1 (Kin1) construct (Kif5A, residues 1-340, in pET151-D-TOPO® (Invitrogen, with a TEV protease-cleavable N-terminal His_6-tag)) was expressed recombinantly in *E. coli* and purified using cobalt affinity chromatography. The His_6-tag was removed by cleavage with TEV protease and the untagged protein was buffer exchanged into BrB20 buffer (20mM PIPES, 2mM $MgCl_2$, 1mM EGTA, 2mM DTT, pH6.8). A human kinesin-3 (Kin3) construct (Kif1A, residues 1-361, in pFN18a (with a TEV protease-cleavable N-terminal Halo-tag and a C-terminal His_6-tag (a kind gift from Prof. Christopher A. Walsh's laboratory, Harvard Medical School), was expressed recombinantly in *E. coli* and purified using nickel affinity chromatography and size exclusion chromatography (GE Healthcare Life Science, Superdex 75). The N-terminal Halo-tag was removed by cleavage with TEV protease, the sample was dialyzed into storage buffer (20 mM HEPES, pH 7, 150 mM NaCl, 1 mM TCEP, 5 mM $MgCl_2$, and 0.1 mM ADP) and concentrated. Note that this construct contains the native Kin3 (Kif1A) sequence, as opposed to several previous studies where a chimeric protein with substitution of its neck linker with that of the kinesin-1 Kif5C (Kikkawa and Hirokawa, 2006; Kikkawa et al., 2001; Nitta et al., 2004; Nitta et al., 2008). The steady state MT-activated ATPase activities of our motor constructs were determined by measuring phosphate production with a commercially available kit (EnzChek, Molecular Probes). Assays contained 10nM motor domain and a minimum of 4-fold molar excess of paclitaxel-stabilised MTs in 50mM K-acetate, 25mM HEPES, 5mM Mg-acetate, 1mM EGTA, pH7.5 at 20°C. The dependence of rates of inorganic phosphate production on [MT] and [ATP] were fitted with a Michaelis-Menten relationship (Table 3).

Microtubule preparation

Bovine tubulin (Cytoskeleton Inc) at a final concentration of 50μM in MT polymerization buffer (100mM MES pH 6.5, 1mM $MgCl_2$, 1mM EGTA, 1mM DTT, 5mM GTP) was polymerized at 37°C for 1 hour. 1mM paclitaxel (Calbiochem) in DMSO was then added, and the sample was incubated at 37°C for a further hour.

Cryo-EM sample preparation

MTs were diluted in BrB20 to a final concentration of 5μM. Kin1 and Kin3 were diluted in BrB20 containing either 2mM of AMPPNP, ADP, ADP + AlF_4 or apyrase (10 units/mL), according to established protocols (Fourniol and Moores, 2011; Hirose and Amos, 2007; Sindelar and Downing, 2007, 2010), and warmed to room temperature 10 minutes prior to complex formation. The final concentrations used to visually achieve full decoration in the various

nucleotide states are shown in Table 4. C-flat™ holey carbon grids (Protochips) with 2μm holes and 4μm spacing were glow-discharged in air. 4ul drops of MT then Kin1 or Kin3 samples were added and blotted in sequential fashion using a Vitrobot plunge-freezing device (FEI Co.) operating at 25°C and 100% humidity, and vitrified in liquid ethane.

Data Collection

Images of MT-kinesin complexes were collected using a 4kx4k CCD camera (Gatan Inc.) on a FEI Tecnai G2 Polara operating at 300kV with a calibrated magnification of 100,000x, and a final sampling of 1.5Å/pixel. A defocus range of 0.4-3.5μm and an electron dose of ~20e^-/Å^2 were used. Images were screened manually to remove those with drift and/or objective astigmatism, contamination, and not containing at least one fully decorated and straight 13 protofilament MT.

Data Processing

Kinesin-decorated straight 13 protofilament MT segments were manually boxed using Eman suite's Boxer (Ludtke et al., 1999) and input to a set of custom-designed semi-automated single-particle processing scripts using Spider (Frank et al., 1996) and Frealign (Grigorieff, 2007) as described previously (Sindelar and Downing, 2007, 2010), with minor modifications during local refinement. The phi-angle and thus seam location is determined in pseudo-symmetrical 13 protofilament MTs using projection matching in Spider (Frank et al., 1996). Once approximate alignment parameters are determined and manually verified (based on known values for the MT lattice), local refinement and CTF correction is performed in Frealign (Grigorieff, 2007). Eight rounds of refinement were undertaken and a negative Bfactor of -400 was applied to the output reconstruction of round five to escape local minima in the search space; no Bfactor was applied in the following three rounds to reduce possible over-fitting (http://grigoriefflab.janelia.org/forum). The angular distribution was isotropic for all data sets and the final reconstructions of the asymmetric unit (αβ-tubulin heterodimer + kinesin motor domain) were generated using 13 protofilament MT pseudo-symmetry. All final maps were assessed for possible over-fitting during refinement using a high-resolution noise-substitution test (Chen et al., 2013). Final estimated resolutions for each reconstruction are reported in Table 1 and FSC curves are shown in Figure 1 – figure supplement 1. Band-pass filtering of these reconstructions using a Fermi temperature of 0.04 was performed in Spider (Frank et al., 1996) between frequencies of 15-6Å (except for K1 Mg-ADPAlFx-MT reconstruction, where 15-7Å was used).

Atomic Structure Fitting and Refinement

50 initial atomic models of each motor domain (in each nucleotide state) were built using Modeller v9.12 (Sali and Blundell, 1993) based on multiple template structures (see Table 2). Initial fitting of each model into the respective maps was done using the Chimera *fit_in_map* tool (Goddard et al., 2007). The best model was selected based on a combination of the cross correlation coefficient (CCC) between each model and the density map and a statistical potentials score (zDOPE; (Shen and Sali, 2006). Each map was box-segmented around the motor domain and the EM density for the tubulin was masked out (using Chimera *volume eraser* tool). The best fits were further refined with Flex-EM following a multistep optimisation protocol relying on simulated annealing molecular dynamics and a conjugate-gradients minimization applied to a series of subdivisions of the structure into rigid bodies (Topf et al., 2008) as identified by RIBFIND (Table 2, (Pandurangan and Topf, 2012). In order to analyse subtle conformational changes occurring in various regions of the domain in the different nucleotide states, the quality of the final fits was assessed locally with TEMPy (Farabella et al., in revision) using the segment based cross correlation coefficient (SCCC, Figure 1 – figure supplement 2) (Pandurangan et al., 2014).

Acknowledgments

The authors thank Charles Sindelar (Yale University, USA) for reconstruction algorithms, members of the Birkbeck EM group for helpful discussions, the MRC (MR/J000973/1; to JA, CAM), NIGMS (RO1GM102875-07; to SR), BBSRC (BB/K01692X/1; to IF, MT) and CNRS, la Ligue contre le Cancer Comité de Paris, ARC SFI20121205398 and the Fédération pour la Recherche sur le Cerveau (FRC; AH and I-MY) for funding. I-MY is a recipient of a Marie Curie IIF Fellowship. The team of AH is part of Labex Deep:11-LBX-0044

Author contributions

JA, Conception and design, Acquisition of data, Analysis and interpretation of data, Drafting or revising the article; IF, Analysis and interpretation of data, Drafting or revising the article; I-MY, Acquisition of data, Analysis and interpretation of data, Drafting or revising the article; SSR, Acquisition of data, Analysis and interpretation of data, Drafting or revising the article; AH, Analysis and interpretation of data, Drafting or revising the article; MT, Analysis and interpretation of data, Drafting or revising the article; CAM, Conception and design, Analysis and interpretation of data, Drafting or revising the article.

Competing interests

The authors declare that no competing interests exist.

FIGURE LEGENDS

Figure 1: Overview of MT-bound kinesin motor domain cryo-EM reconstructions. A) Example cryo-EM image of kinesin-decorated MT (Kin1_Mg-AMPPNP); blue arrows indicate individual Kin1 motor domains. B) Example of cryo-EM reconstruction of 13 protofilament, kinesin-decorated MT (Kin1-Mg-AMPPNP); blue arrows indicate individual Kin1 motor domains, and the dotted red box shows an asymmetric unit. A single protofilament is indicated, along with the position of the lattice seam. C) Example of an individual asymmetric unit (Kin1-Mg-AMPPNP), contoured to show secondary structural elements. D) Two views, related by 180º, of an exemplar pseudo-atomic model (Kin1-Mg-AMPPNP) calculated using our cryo-EM reconstruction. The major mechanochemical elements discussed in the text are colour-coded as indicated in the key.

Figure 2. Conserved conformations at the nucleotide-binding pocket in Kin3s and Kin1s. A-C) The nucleotide-binding pocket of MT-bound Kin3 reconstructions (shown as blue transparent density) in A) Mg-ADP, model shown in light blue; the arrowhead indicates residual flexibility in the helix-α4 N-terminus and the region of loop11 for which density is missing is depicted by a dotted red line; B) no nucleotide (NN), model shown in mid-blue; density connects the C-terminal helical turn of loop11 with the MT (arrow), density corresponding to the rest of loop11 is seen (chevron) and density now connects the extended loop 9 and the P-loop (arrowhead); C) Mg-ADPAlFx, model shown in dark blue; the C-terminal helical turn of loop11 has moved away from the MT (arrow) and strong density is seen connecting it, helix-α4 and loop9 around the bound nucleotide. D-E) The nucleotide-binding pocket of MT-bound Kin1 reconstructions (shown as green transparent density) in D) no nucleotide, model shown in light green; density connects the C-terminal helical turn of loop11 with the MT (arrow), density corresponding to the majority of loop11 is seen (chevron) and density now connects the extended loop 9 and the P-loop (arrowhead); E) Mg-AMPPNP, model shown in dark green; the C-terminal helical turn of loop11 has moved away from the MT (arrow) and strong density is seen connecting it, helix-α4 and loop9 around the bound nucleotide. In all reconstructions, density for the motor domain was contoured to an equivalent volume.

Figure 3. Conserved conformational changes of helix-α6 alter MT connectivity and allow neck linker docking on Mg-ATP binding. A-C) View of helix-α6 and the neck linker (in fuchsia) of MT-bound Kin3 reconstructions (shown as blue transparent density) in A) Mg-ADP, model shown in light blue, B) no nucleotide (NN), model shown in mid-blue, C) Mg-ADPAlFx, model shown in dark blue; D-E) View of helix-α6 and the neck

linker (in fuchsia) of MT-bound Kin1 reconstructions (shown as green transparent density) in D) no nucleotide, model shown in light green, E) Mg-AMPPNP, model shown in dark green. In Mg-ADP (Kin3) and NN states (both motors), helix-α6 contacts the surface of α-tubulin (arrowhead) and its orientation with respect to helix-α4 ensures that the neck linker cannot dock. Regions of density at the C-terminal end of helix-α6, likely representing conformers of the N-terminal portion of the neck linker are observed (arrows), although the majority is not visible, presumably due to flexibility. In both motors, peeling of the motor domain β-sheet core away from helix-α4 upon Mg-ATP binding allows rotation and extension of helix-α6, drawing it away from the MT surface (arrowhead), and allowing it to occupy the space between helix-α4 and the β-sheet core. The neck linker docks towards the MT plus end (arrow) and forms the CNB with the N-terminus (in orange). In all reconstructions, density for the motor domain was contoured to an equivalent volume.

Figure 4. Nucleotide-independent interactions between the kinesin motor domain and the MT surface. A-C) View from the MT plus end of the motor domain-MT interface in MT-bound Kin3 reconstructions (shown as blue transparent density) in A) Mg-ADP, model shown in light blue, B) no nucleotide (NN), model shown in mid-blue, C) Mg-ADPAlFx, model shown in dark blue, in which the CNB is formed between the neck linker (fuchsia) and N-terminus (orange). The N-terminus of loop12 (light pink) extends helix-α4 by a turn but the central, lysine-rich portion of this loop is not visible (dotted pink line), nor is the β-tubulin CTT (arrowhead) with which it is known to interact. Loop8/strand-β5 form a clear connection to the MT surface (arrow). D-E) The same view of the motor domain-MT interface in MT-bound Kin1 reconstructions (shown as green transparent density) in D) no nucleotide, model shown in light green, E) Mg-AMPPNP, model shown in dark green, in which the CNB is formed between the neck linker (fuchsia) and N-terminus (orange). The shorter Kin1 loop12 is clearly visualised and contacts the MT surface while loop8/strand-β5 are not connected by density to the MT surface (arrow). In all reconstructions, density for the motor domain was contoured to an equivalent volume.

Figure 5: Transmission of force generation across the motor domain on Mg-ATP binding. A,B) Conformational changes relative to superposition of the core β-sheet of Kin3 (A) and Kin1 (B) showing the RMSDs due to Mg-ATP binding coloured from yellow (no change) to pink (large change), depicted on the Mg-ATP-like structures. Note, because the core β-sheet moves relative to helix-α4, which is held at the MT interface, alignment of the β-sheet artificially shows large displacements of helix-α4 and other nucleotide-invariant MT contacts at the back of this view. C,D) Comparison of the nucleotide-binding

site before and after Mg-ATP binding in Kin3 (C) and Kin1 (D). In each case, the NN model is depicted within the Mg-ATP cryo-EM density and shows that the regions of the largest RMSDs (pink in panels A and B) correspond to regions of the models that clearly do not fit in the density, i.e. that undergo conformational changes when Mg-ATP binds.

Figure 6: Comparison of Kin3 and Kin1. A) Sequence alignment of Kin3 (Kif1A) and Kin1 (Kif5A) motor domains showing secondary structural elements within the domains, annotated according to sequence and charge conservation. Elements depicted in other panels are underlined. B) Longitudinal slice through the Kin3-NN model viewed from the front showing the MT contact elements and the underlying structural regions in αβ-tubulin. C) MT binding surface of Kin3-NN model viewed from the MT surface (180º rotated compared to B) annotated by sequence identity (black) between Kin3 and Kin1 and sequence insertions (green). Structural elements in the MT are removed in this view to most clearly show elements in the motor domain. D) MT binding surface of Kin3-NN model showing the differences in charge (blue: Kin3 more acidic than Kin1; red: Kin3 more basic than Kin1); same view as in C.

Figure 7. Model of conserved MT-bound kinesin mechanochemistry. Loop11/N-terminus of helix-α4 are flexible in ADP-bound kinesin in solution, the neck linker is also flexible while loop9 chelates ADP. MT binding is sensed by loop11/helix-α4 N-terminus, biasing them towards more ordered conformations. We propose that this favours crosstalk between loop11 and loop9, stimulating ADP release. In the NN conformation, both loop11 and loop9 are well ordered and primed to favour ATP binding, while helix-α6 – which is required for mechanical amplification - is closely associated with the MT on the other side of the motor domain. ATP binding draws loop11 and loop9 closer together; causing: 1) tilting of most of the motor domain not contacting the MT towards the nucleotide-binding site, 2) rotation, translation and extension of helix-α6 which we propose contributes to force generation and 3) allows neck linker docking and biases movement of the 2nd head towards the MT plus end.

TABLES

Kinesin and nucleotide state	Number of AU	FSCt 0.5 (0.143)	FSCtrue 0.5 (0.143)	Rmeasure 0.5 (0.143)	EMDB accession number
Kin3-Mg-ADP	181,311	7.9 (6.3)	8 (7)	8.1 (7.5)	EMD-2768
Kin3-NN	187,538	7.4 (6.3)	7.5 (6.3)	7.8 (6.9)	EMD-2765
Kin3-Mg-AMPPNP	97,877	8.1 (6.9)	8.2 (7.0)	8 (7.3)	EMD-2766
Kin3-Mg-ADPAlFx	156,845	7.9 (6.8)	8.3 (7.0)	8 (7.3)	EMD-2767
Kin1-NN	168,974	8.2 (7.2)	8.3 (7.4)	8.3 (7.3)	EMD-2769
Kin1-Mg-AMPPNP	186,329	7.3 (6.0)	7.5 (6.5)	7.7 (6.9)	EMD-2770
Kin1-Mg-ADPAlFx	65,572	9 (7.3)	9.1 (7.7)	9.1 (8.1)	EMD-2771

Table 1. Data set size and estimated reconstruction resolutions. For each reconstruction, the motor domain and nucleotide state, number of asymmetric units (AU) in the final reconstruction, the resolutions at a cut-off of 0.5 and 0.143 estimated by standard FSC (FSCt) and that corrected with the HRnoise substitution test (FSCtrue) (Chen et al., 2013) and by Rmeasure (Sousa and Grigorieff, 2007) and the EMDB accession number are given.

Kinesin and nucleotide state	Models used	CCC initial model	CCC final model	PDB code
Kin3-Mg-ADP	1VFZ (Nitta et al., 2004) 1I5S (Kikkawa et al., 2001) 4AQW (Goulet et al., 2012)	0.66	0.68	4uxs
Kin3-NN	1VFZ/1I5S/4HNA (Gigant et al., 2013)/4AQW	0.63	0.68	4uxo
Kin3-Mg-AMPPNP	1VFV (Nitta et al., 2004) 4HNA	0.72	0.75	4uxp
Kin3-Mg-ADPAlFx	1VFV/4HNA	0.74	0.75	4uxr
Kin1-NN	1BG2 (Kull et al., 1996)/4HNA/ 4AQW	0.71	0.73	4uxt
Kin1-Mg-AMPPNP	4HNA	0.73	0.76	4uxy
Kin1-Mg-ADPAlFx	4HNA	0.69	0.72	4uy0

Table 2. Calculation of pseudo-atomic models. A set of starting models were used for each nucleotide state of each motor. Flexible fitting and further refinement were performed using Flex-EM and Modeller (see Methods). Global CCCs of models with their respective reconstructions were calculated

using the *Fit In Map* tool in Chimera. PDB accession codes for the final models are also shown.

	Kin3 (Kif1A)	Kin1 (Kif5A)
k_{cat} (s^{-1})	43.4 ± 1.0	34.2 ± 5.7
$K_{0.5ATP}$ (μM)	30 ± 10	25 ± 5
$K_{0.5\ MT}$ (nM)	53.7 ± 5.7	12745 ± 4041

Table 3. Steady-state MT-activated ATPase parameters of our Kin3 and Kin1 motor domain constructs.

Kinesin and nucleotide state	[MT] (μM)	[motor domain] (μM)
Kin3 MgADP	5	10
Kin3 NN	5	5
Kin3 Mg-AMPPNP	5	5
Kin3 Mg-ADP.AlFx	5	5
Kin1 NN	5	100
Kin1 Mg-AMPPNP	5	50
Kin1 Mg-ADP.AlFx	5	50

Table 4. Final protein concentrations used for cryo-EM sample preparation. Kin1 samples required higher concentrations than Kin3 to achieve good MT occupancy.

Supplementary Figures Legends

Figure 1

Figure 1 – figure supplement 1. Resolution estimation for cryo-EM reconstructions. For each reconstruction, three Fourier Shell Correlation (FSC) curves are plotted: standard FSCt (blue) between two half data sets, FSCn (noise substitution cutoff 10Å, red) and FSCtrue (green, see Chen et al., 2013). A) Kin3-Mg-ADP-MT, B) Kin3-NN-MT, C) Kin3-Mg-AMPPNP-MT, D) Kin3-Mg-ADPAlFx-MT, E) Kin1-NN-MT, F) Kin1-Mg-AMPPNP-MT, G) Kin1-Mg-ADPAlFx-MT. Dotted lines indicate estimated resolution by FSCtrue at 0.143 (considered appropriate for FSCtrue) and 0.5 criteria. The overall good agreement between FSCt and FSCtrue curves demonstrates that minimal over-fitting occurred during refinement of the cryo-EM data.

Figure – figure supplement 2. Local assessment of fit quality of the pseudo-atomic models within the cryo-EM density. Following flexible fitting of each kinesin motor domain, the local fit quality of specific elements was calculated. A,B) NN cryo-EM density for A) Kin3 and B) Kin1 are shown with their respective docked pseudo-atomic model colour-coded according to segment based cross correlation coefficient (SCCC, see colour key; (Pandurangan et al., 2014). C, D) Heat map showing the quality of the local fit for specific elements of the motor domain in different nucleotide states for (C) Kin3 and (D) Kin1. The colour (see key) denotes the SCCC score as calculated with TEMPy (Farabella et al, in revision). This analysis shows the quality of the fits and provides confidence in our interpretation of conformational changes in these regions. In particular, it shows that loop9 and loop11 have similar (good) quality of fit compared to the α-helices, apart from loop11 in the Kin3-Mg-ADP reconstruction, for which cryo-EM density was not seen.

Figure 2

Figure 2 – figure supplement 1. Conserved conformations at the nucleotide-binding pocket in Kin3 and Kin1 alternative ATP-like states. A) The nucleotide-binding pocket of the MT bound Kin3-Mg-AMPPNP (blue transparent density and navy blue model). B) The nucleotide-binding pocket of the MT bound Kin1-Mg-ADPAlFx reconstruction (green transparent density and olive green model). The major features are shared by all the ATP-like reconstructions: in Kin3-Mg-AMPPNP the C-terminal helical turn of loop11 has moved away from the MT (arrow) and strong density (arrowhead) is seen connecting it, helix-α4 and loop9 around the bound nucleotide. The Kin1-Mg-ADPAlFx reconstruction is lower resolution (FSCtrue, 0.143 = 7.7), which may explain why residual density connects the C-terminal helical turn of loop11 with the MT (arrow); however strong density is seen connecting it, helix-α4

and loop9 around the bound nucleotide. In all reconstructions, density for the motor domain was contoured to an equivalent volume.

Figure 2 – figure supplement 2. Coordination of Mg-ADP cluster by loop9 and loop11. A) Sequence alignment of Kin3 and Kin1 highlighting conserved Mg-water 'cap' coordinating residues (magenta squares above residue letters) in loop9 (yellow shading) and near loop11 (red shading). B) The crystal structure of Kin3-Mg-ADP (Kif1A; PDB 1I5S; Kikkawa et al., 2001) showing the side-chains of the residues (Kin3: Arg203, Ser214, Ser215, Asp248) indicated in panel A. Putative hydrogen bonds (displayed with *FindHBond* Chimera plugin) between these residues and the Mg-water cap are shown as solid magenta lines. Water molecules and Mg are shown as red and green spheres respectively. We propose that MT-triggered displacement of loop9 leads to destabilization of the Mg-water cap and consequent Mg-ADP release from the nucleotide pocket.

Figure 2 – figure supplement 3. Conserved residues involved in MT-mediated stimulation of Mg-ADP release. A) Sequence alignment of Kin3 and Kin1 highlighting residues likely to be important in MT-mediated stimulation of Mg-ADP release. Residues involved in MT sensing and stabilization of loop11 are indicated by purple squares above residue letters (Kin3 residue number), whereas those involved in communication between loop11 (at the MT) and loop9 (water-Mg-ADP coordination) are indicated by magenta squares. Loop9 is indicated by yellow shading, loop11 by red shading, and the P-loop by brown shading. B,C) Location of these residues in the NN-MT-bound models of B) Kin3 (mid blue) within the equivalent reconstruction (blue transparent density) and C) Kin1 (light green) within the equivalent reconstruction (green transparent density), contoured at equivalent volumes. We propose that MT binding reduces the conformational freedom of loop11, stabilizing a helical turn that involves Kin3 Ala255 (Kin1 Val238) and Ala260 (Kin1 Ala244), and Kin3 Thr258 (Kin1 Thr242) above α-tubulin's H3'. Kin3 helix-α4 Asn272 (Kin1 Asn256) sits at the interface of α-tubulin and loop11, likely interacting with both (Gigant et al., 2013) and presumably stabilizing loop11. Kin3 loop11 Arg254 (Kin1 Lys238) may help stabilize loop11 through its interaction with the acidic tip of α-tubulin's H12 (Gigant et al., 2013). Communication between loop11 and loop9 likely occurs via a salt bridge between Kin3 loop Glu253 (Kin1 Glu237) and loop9 Arg216 (Kin1 Arg204) as reported in hydrolysis-competent conformation ATP-like crystal structures (Chang et al., 2013; Gigant et al., 2013; Parke et al., 2010). Kin3 helix-α4 Glu267 (Kin1 Glu251) also interacts with loop9 Arg216 (Kin1 Arg204), an interaction that also involves loop7 Tyr150 (Kin1 Tyr139; Liu et al., 2012a). Evidence for these residues involvement in MT-mediated Mg-ADP release is provided by structural and biochemical studies and disease-causing

patient mutations (*Nitta et al., 2008; ♤Woehlke et al, 1997; ‡Yun et al, 2001; §Ebbing et al., 2008; ¶Song & Endow, 1998; // Liu et al., 2012).

Figure 2 – figure supplement 4. Structural routes of communication between the nucleotide-binding pocket and helix-α6 for mechanochemical coupling. A) Sequence alignment of Kin3 and Kin1 highlighting residues involved in communication from the nucleotide-binding pocket to helix-α6. Residues involved in loop9-loop11 communication are indicated by magenta squares above residue letters and loop11-helix-α6 communication by orange squares above residue letters. Residue numbers for Kin1 (Kif5A) are indicated. Loop9 is indicated by yellow shading, loop11 by red shading, and the P-loop by brown shading. B) The crystal structure of tubulin dimer-bound Kin1-Mg-ADPAlFx (Kif5B; PDB 4HNA) focusing on the residues indicated in panel A. Residue numbers for Kif5A are indicated. The close association of loop9 and loop11 in ATP-like crystal structures (Chang et al., 2013; Gigant et al., 2013; Parke et al., 2010) involves backbone hydrogen bonds between loop9 Asn197 and loop11 Thr242, and also involves Met198. Residues in loop11 (Lys241, Lys238 in Kin1, Arg264 in Kin3) interact with the base of helix-α6 (Asn310, Glu313 in Kin1, Asn337, Glu340 in Kin3). P-loop residues in Kin1 (Tyr85, Gln87; Kin3 Tyr96, Gln98) also interact with helix-α6. We propose that these interactions will form in the transition from NN to Mg-ATP bound (Figure 2) and will contribute to mechanical transmission (Figure 3).

Figure 2 – figure supplement 5. Occupancy of the nucleotide pocket. Similar views of the nucleotide-binding pocket aligned on the P-loop are shown for each reconstruction, with the corresponding model fitted into density; A) Kin3-Mg-ADP, B) Kin3-NN, Kin3-Mg-AMPPNP, D) Kin3-Mg-ADPAlFx, E) Kin1-NN, F) Kin1-Mg-AMPPNP, G) Kin1-Mg-ADPAlFx. The presence or absence of density in the nucleotide-binding pocket is consistent with the sample preparation used for each reconstruction and supports their interpretation. H) The Kin3-Mg-ADP model is shown in the Kin3-NN reconstruction, clearly demonstrating the lack of density in the nucleotide-pocket to accommodate Mg-ADP (arrow) and supporting our assignment of this structure as nucleotide-free. The opacity of all reconstructions in this figure has been increased in order to more clearly illustrate the boundary of the EM density compared to the docked model. The contouring is the same as in all other figures.

Figure 3

Figure 3 – figure supplement 1. Conserved conformation of helix-α6 allows neck linker docking on Mg-ATP binding in Kin3 and Kin1 alternative ATP-like states. A) View of helix-α6 and the neck linker (in

fuchsia) of MT bound Kin3-Mg-AMPPNP (blue transparent density and navy blue model). B) View of helix-α6 and the neck linker (in fuchsia) of MT bound Kin1_Mg-ADPAlFx reconstruction (green transparent density and olive green model). The major features are shared by all the ATP-like reconstructions: in both motors, peeling of the motor domain β-sheet core on Mg-ATP binding allows rotation and extension of helix-α6, drawing it away from the MT surface (arrowhead). The neck linker docks towards the MT plus end (arrow) and forms the CNB with the N-terminus (in orange). In all reconstructions, density for the motor domain was contoured to an equivalent volume.

Figure 3 – figure supplement 2. Tilting of the core β-sheet on Mg-ATP binding in Kin1 and Kin3 causes peeling of the β-sheet from the C-terminus of helix-α4 to allow movement and extension of helix-α6 and neck linker docking. In each panel, a stripped-down depiction of each pseudo-atomic model is presented showing helix-α4, adjacent loops (shown for orientation) and the core β-sheet, viewed from the MT minus end. A) MT bound Kin3-NN; B) MT bound Kin3-ATP-like; C) MT bound Kin3-NN; D) Kin-ATP-like. In each case, the distance between the backbone Cα of conserved residues at the helix-α4 C-terminus and the immediately overlying β-sheet region were measured in Chimera (indicated in pink). The tilt of each β-sheet upon ATP-analogue binding was calculated by measuring the change in angle between helix-α4 and the β-sheet using the *Axes/Planes/Centroids* tool in Chimera.

Figure 3 – figure supplement 3. Conserved conformational changes of helix-α6 relative to helix-α4 control neck-linker docking along the core β-sheet when Mg-ATP binds. A-D) View towards the MT with the plus end towards the top of MT-bound Kin3 reconstructions (shown as blue transparent density) in A) Mg-ADP, model shown in light blue, B) no nucleotide (NN), model shown in the mid-blue, C) Mg-AMPPNP, model shown in navy blue, and D) Mg-ADPAlFx, model shown in dark blue; E-G) Same view of MT-bound Kin1 reconstructions (shown is green transparent density in E) no nucleotide (NN), model shown in light green, F) Mg-AMPPNP, model shown in dark green, G) Mg-ADPAlFx, model shown in olive green. In Mg-ADP/NN states of Kin3 (A and B) and the NN state of Kin1 (E) helix-α6 terminates before helix-α4 leaving a gap (chevrons). Additional regions of density (arrows) at the helix-α6 C-terminus likely represent conformers of the initial portion of the neck linker (fuchsia), most of which is invisible and presumably flexible. However, in AMPPNP/ADPAlFx states of both Kin3 (C and D) and Kin1 (F and G), tilting of the motor domain allows helix-α6 to extend, closing the gap between helix-α4 and allowing neck linker docking, for which extra density is seen alongside the core β-sheet (arrowheads). Neck linker docking

allows CNB formation with the N-terminus (orange). In all reconstructions, density for the motor domain was contoured to an equivalent volume.

Figure 4

Figure 4 – figure supplement 1. Conserved conformations at the kinesin motor domain **and the MT surface in Kin3 and Kin1 alternative ATP-like states.** A) View from the MT plus end of the motor domain-MT interface in the MT bound Kin3-Mg-AMPPNP (blue transparent density and navy blue model). B) View from the MT plus end of the motor domain-MT interface in the MT bound Kin1-Mg-ADPAlFx reconstruction (green transparent density and olive green model). The major features are shared by all the ATP-like reconstructions: The CNB is formed between the neck linker (fuchsia) and N-terminus (orange). The N-terminus of loop12 (light pink) extends helix-α4 by a turn but the central, lysine-rich portion of this loop is not visible (dotted pink line), nor is the β-tubulin CTT (arrowhead) with which it is known to interact. Loop8/strand-β5 form a clear connection to the MT surface (arrow). The Kin1-Mg-ADPAlFx reconstruction is lower resolution (FSCtrue, 0.143 = 7.7), which may explain why residual density connects Loop8/strand-β5 and the MT surface, which is not the case in the Kin1-Mg-AMPPNP reconstruction (Figure 4E). In all reconstructions, density for the motor domain was contoured to an equivalent volume.

Figure 5

Figure 5 – figure supplement 1. Limited β-sheet flexure during kinesin ATPase cycle compared to myosin5. Superposition of the core β-sheets of motor domains in different nucleotide states reveals subtle differences at their edges, indicating β-sheet flexure at each transition. On the left of each panel, the core β-sheets of A) Kin3-Mg-ADP-MT and Kin3-NN-MT, B) Kin3-NN-MT and Kin3-Mg-ADPAlFx-MT, C) Kin1-NN-MT and Kin1-Mg-AMPPNP-MT models are shown superimposed, viewed from the MT minus end. D) For comparison Myosin5-NN (PDB 1OE9) and Myosin5 Mg-ADP-BeFx ATP-like (PDB 1W7J) crystal structures are shown superimposed, where β-sheet flexure has been shown to occur (Coureux et al., 2003; Reubold et al., 2003). Arrowheads indicate the tip of loop7 and arrows indicate strand-β3 (which connects to the P-loop), or the structurally equivalent region in the Myosin motor domain (indicated with *). On the right of each panel, the corresponding RMSDs of each overlay are shown, displayed using a scale from 0 (yellow) to pink (3.2Å). The motor domain MT minus end is to the left and plus end, that contains the flexible loop10, to the right. A) Kin3 Mg-ADP release: maximum loop7 RMSD ~1.6Å; B) Kin3 Mg-ATP binding: loop7, RMSD ~2.5Å, strand-β3: RMSD ~1.7Å; C) Kin1 Mg-ATP binding: loop7, RMSD ~1.8Å, strand-β3: RMSD ~1.2Å; D) Myosin5 Mg-ADP release: loop7* maximum RMSD ~3.3Å (Coureux et al., 2003; Reubold et al., 2003).

Figure 5 – figure supplement 2. Pincer-like closure of loop9 and loop11 contributes to motor domain tilt when ATP binds. A) MT binding and Mg-ADP release in the Kin3-NN-MT, viewed from the MT minus end, induce an ordered loop9 and loop11 conformation; B) ATP-binding induces loop9 and loop11 to move together contributing to motor domain tilting towards the bound nucleotide, thereby enabling neck linker docking. C,D) The same conformational changes are seen in Kin1. Red and yellow arrows represent the 'pincer'-like movement of loop9 and loop11 towards each other that produces the new density connection between them. Tilting of the motor domains relative to helix-α4 is indicated with orange curved arrows.

References

Alonso, M.C., van Damme, J., Vandekerckhove, J., and Cross, R.A. (1998). Proteolytic mapping of kinesin/ncd-microtubule interface: nucleotide-dependent conformational changes in the loops L8 and L12. EMBO J *17*, 945-951.

Asenjo, A.B., Chatterjee, C., Tan, D., DePaoli, V., Rice, W.J., Diaz-Avalos, R., Silvestry, M., and Sosa, H. (2013). Structural model for tubulin recognition and deformation by kinesin-13 microtubule depolymerases. Cell Rep *3*, 759-768.

Asenjo, A.B., Weinberg, Y., and Sosa, H. (2006). Nucleotide binding and hydrolysis induces a disorder-order transition in the kinesin neck-linker region. Nat Struct Mol Biol *13*, 648-654.

Case, R.B., Pierce, D.W., Hom-Booher, N., Hart, C.L., and Vale, R.D. (1997). The directional preference of kinesin motors is specified by an element outside of the motor catalytic domain. Cell *90*, 959-966.

Case, R.B., Rice, S., Hart, C.L., Ly, B., and Vale, R.D. (2000). Role of the kinesin neck linker and catalytic core in microtubule-based motility. Curr Biol *10*, 157-160.

Chang, Q., Nitta, R., Inoue, S., and Hirokawa, N. (2013). Structural basis for the ATP-induced isomerization of kinesin. J Mol Biol *425*, 1869-1880.

Chen, S., McMullan, G., Faruqi, A.R., Murshudov, G.N., Short, J.M., Scheres, S.H., and Henderson, R. (2013). High-resolution noise substitution to measure overfitting and validate resolution in 3D structure determination by single particle electron cryomicroscopy. Ultramicroscopy *135*, 24-35.

Clancy, B.E., Behnke-Parks, W.M., Andreasson, J.O., Rosenfeld, S.S., and Block, S.M. (2011). A universal pathway for kinesin stepping. Nat Struct Mol Biol *18*, 1020-1027.

Cochran, J.C., Sindelar, C.V., Mulko, N.K., Collins, K.A., Kong, S.E., Hawley, R.S., and Kull, F.J. (2009). ATPase cycle of the nonmotile kinesin NOD allows microtubule end tracking and drives chromosome movement. Cell *136*, 110-122.

Coureux, P.D., Wells, A.L., Menetrey, J., Yengo, C.M., Morris, C.A., Sweeney, H.L., and Houdusse, A. (2003). A structural state of the myosin V motor without bound nucleotide. Nature *425*, 419-423.

Cross, R.A., and McAinsh, A. (2014). Prime movers: the mechanochemistry of mitotic kinesins. Nat Rev Mol Cell Biol *15*, 257-271.

Desai, A., Verma, S., Mitchison, T.J., and Walczak, C.E. (1999). Kin I kinesins are microtubule-destabilizing enzymes. Cell *96*, 69-78.

Ebbing, B., Mann, K., Starosta, A., Jaud, J., Schols, L., Schule, R., and Woehlke, G. (2008). Effect of spastic paraplegia mutations in KIF5A kinesin on transport activity. Hum Mol Genet *17*, 1245-1252.

Farabella, I., Vasishtan, D., Joseph, AP., Pandurangan, A.P., Sahota, H., and Topf, M. (2014). TEMPy: a Python Library for Assessment of 3D Electron Microscopy Density Fits. *In revision.*

Farrell, C.M., Mackey, A.T., Klumpp, L.M., and Gilbert, S.P. (2002). The role of ATP hydrolysis for kinesin processivity. J Biol Chem *277*, 17079-17087.

Fourniol, F.J., and Moores, C.A. (2011). Snapshots of kinesin motors on microtubule tracks. Methods Mol Biol *778*, 57-70.

Frank, J., Radermacher, M., Penczek, P., Zhu, J., Li, Y., Ladjadj, M., and Leith, A. (1996). SPIDER and WEB: processing and visualization of images in 3D electron microscopy and related fields. J Struct Biol *116*, 190-199.

Gigant, B., Wang, W., Dreier, B., Jiang, Q., Pecqueur, L., Pluckthun, A., Wang, C., and Knossow, M. (2013). Structure of a kinesin-tubulin complex and implications for kinesin motility. Nat Struct Mol Biol *20*, 1001-1007.

Goddard, T.D., Huang, C.C., and Ferrin, T.E. (2007). Visualizing density maps with UCSF Chimera. J Struct Biol *157*, 281-287.

Goulet, A., Behnke-Parks, W.M., Sindelar, C.V., Major, J., Rosenfeld, S.S., and Moores, C.A. (2012). The structural basis of force generation by the mitotic motor kinesin-5. J Biol Chem *287*, 44654-44666.

Goulet, A., Major, J., Jun, Y., Gross, S.P., Rosenfeld, S.S., and Moores, C.A. (2014). Comprehensive structural model of the mechanochemical cycle of a mitotic motor highlights molecular adaptations in the kinesin family. Proc Natl Acad Sci U S A *111*, 1837-1842.

Grant, B.J., McCammon, J.A., Caves, L.S., and Cross, R.A. (2007). Multivariate analysis of conserved sequence-structure relationships in kinesins: coupling of the active site and a tubulin-binding sub-domain. J Mol Biol *368*, 1231-1248.

Greber, U.F., and Way, M. (2006). A superhighway to virus infection. Cell *124*, 741-754.

Grigorieff, N. (2007). FREALIGN: high-resolution refinement of single particle structures. J Struct Biol *157*, 117-125.

Hackney, D.D. (1988). Kinesin ATPase: rate-limiting ADP release. Proc Natl Acad Sci U S A *85*, 6314-6318.

Hackney, D.D. (1994). Evidence for alternating head catalysis by kinesin during microtubule-stimulated ATP hydrolysis. Proc Natl Acad Sci U S A *91*, 6865-6869.

1252 Hahlen, K., Ebbing, B., Reinders, J., Mergler, J., Sickmann, A., and Woehlke,
1253 G. (2006). Feedback of the kinesin-1 neck-linker position on the catalytic site.
1254 J Biol Chem *281*, 18868-18877.

1255 Henry, T., Gorvel, J.P., and Meresse, S. (2006). Molecular motors hijacking
1256 by intracellular pathogens. Cell Microbiol *8*, 23-32.

1257 Hirokawa, N., Nitta, R., and Okada, Y. (2009a). The mechanisms of kinesin
1258 motor motility: lessons from the monomeric motor KIF1A. Nat Rev Mol Cell
1259 Biol *10*, 877-884.

1260 Hirokawa, N., Niwa, S., and Tanaka, Y. (2010). Molecular motors in neurons:
1261 transport mechanisms and roles in brain function, development, and disease.
1262 Neuron *68*, 610-638.

1263 Hirokawa, N., and Noda, Y. (2008). Intracellular transport and kinesin
1264 superfamily proteins, KIFs: structure, function, and dynamics. Physiol Rev *88*,
1265 1089-1118.

1266 Hirokawa, N., Noda, Y., Tanaka, Y., and Niwa, S. (2009b). Kinesin
1267 superfamily motor proteins and intracellular transport. Nat Rev Mol Cell Biol
1268 *10*, 682-696.

1269 Hirose, K., Akimaru, E., Akiba, T., Endow, S.A., and Amos, L.A. (2006). Large
1270 conformational changes in a kinesin motor catalyzed by interaction with
1271 microtubules. Mol Cell *23*, 913-923.

1272 Hirose, K., and Amos, L.A. (2007). High-resolution structural analysis of the
1273 kinesin-microtubule complex by electron cryo-microscopy. Methods Mol Biol
1274 *392*, 213-230.

1275 Hwang, W., Lang, M.J., and Karplus, M. (2008). Force generation in kinesin
1276 hinges on cover-neck bundle formation. Structure *16*, 62-71.

1277 Khalil, A.S., Appleyard, D.C., Labno, A.K., Georges, A., Karplus, M., Belcher,
1278 A.M., Hwang, W., and Lang, M.J. (2008). Kinesin's cover-neck bundle folds
1279 forward to generate force. Proc Natl Acad Sci U S A *105*, 19247-19252.

1280 Kikkawa, M., and Hirokawa, N. (2006). High-resolution cryo-EM maps show
1281 the nucleotide binding pocket of KIF1A in open and closed conformations.
1282 EMBO J *25*, 4187-4194.

1283 Kikkawa, M., Okada, Y., and Hirokawa, N. (2000). 15 A resolution model of
1284 the monomeric kinesin motor, KIF1A. Cell *100*, 241-252.

1285 Kikkawa, M., Sablin, E.P., Okada, Y., Yajima, H., Fletterick, R.J., and
1286 Hirokawa, N. (2001). Switch-based mechanism of kinesin motors. Nature *411*,
1287 439-445.

1288 Konishi, Y., and Setou, M. (2009). Tubulin tyrosination navigates the kinesin-1
1289 motor domain to axons. Nat Neurosci *12*, 559-567.

1290 Kull, F.J., and Endow, S.A. (2013). Force generation by kinesin and myosin
1291 cytoskeletal motor proteins. J Cell Sci *126*, 9-19.

1292 Kull, F.J., Sablin, E.P., Lau, R., Fletterick, R.J., and Vale, R.D. (1996). Crystal
1293 structure of the kinesin motor domain reveals a structural similarity to myosin.
1294 Nature *380*, 550-555.

1295 Liu, H.L., Hallen, M.A., and Endow, S.A. (2012a). Altered nucleotide-
1296 microtubule coupling and increased mechanical output by a kinesin mutant.
1297 PLoS One *7*, e47148.

1298 Liu, J.S., Schubert, C.R., Fu, X., Fourniol, F.J., Jaiswal, J.K., Houdusse, A.,
1299 Stultz, C.M., Moores, C.A., and Walsh, C.A. (2012b). Molecular basis for
1300 specific regulation of neuronal kinesin-3 motors by doublecortin family
1301 proteins. Mol Cell *47*, 707-721.

1302 Ludtke, S.J., Baldwin, P.R., and Chiu, W. (1999). EMAN: semiautomated
1303 software for high-resolution single-particle reconstructions. J Struct Biol *128*,
1304 82-97.

1305 Ma, Y.Z., and Taylor, E.W. (1997). Kinetic mechanism of a monomeric kinesin
1306 construct. J Biol Chem *272*, 717-723.

1307 Mandelkow, E., and Mandelkow, E.M. (2002). Kinesin motors and disease.
1308 Trends Cell Biol *12*, 585-591.

1309 Moores, C.A., Yu, M., Guo, J., Beraud, C., Sakowicz, R., and Milligan, R.A.
1310 (2002). A mechanism for microtubule depolymerization by KinI kinesins. Mol
1311 Cell *9*, 903-909.

1312 Nakata, T., and Hirokawa, N. (1995). Point mutation of adenosine
1313 triphosphate-binding motif generated rigor kinesin that selectively blocks
1314 anterograde lysosome membrane transport. J Cell Biol *131*, 1039-1053.

1315 Nitta, R., Kikkawa, M., Okada, Y., and Hirokawa, N. (2004). KIF1A alternately
1316 uses two loops to bind microtubules. Science *305*, 678-683.

1317 Nitta, R., Okada, Y., and Hirokawa, N. (2008). Structural model for strain-
1318 dependent microtubule activation of Mg-ADP release from kinesin. Nat Struct
1319 Mol Biol *15*, 1067-1075.

1320 Okada, Y., and Hirokawa, N. (1999). A processive single-headed motor:
1321 kinesin superfamily protein KIF1A. Science *283*, 1152-1157.

1322 Okada, Y., and Hirokawa, N. (2000). Mechanism of the single-headed
1323 processivity: diffusional anchoring between the K-loop of kinesin and the C
1324 terminus of tubulin. Proc Natl Acad Sci U S A *97*, 640-645.

1325 Pandurangan, A.P., Shakeel, S., Butcher, S.J., and Topf, M. (2014).
1326 Combined approaches to flexible fitting and assessment in virus capsids
1327 undergoing conformational change. J Struct Biol *185*, 427-439.

1328 Pandurangan, A.P., and Topf, M. (2012). Finding rigid bodies in protein
1329 structures: Application to flexible fitting into cryoEM maps. J Struct Biol *177*,
1330 520-531.

1331 Parke, C.L., Wojcik, E.J., Kim, S., and Worthylake, D.K. (2010). ATP
1332 hydrolysis in Eg5 kinesin involves a catalytic two-water mechanism. J Biol
1333 Chem *285*, 5859-5867.

1334 Peters, C., Brejc, K., Belmont, L., Bodey, A.J., Lee, Y., Yu, M., Guo, J.,
1335 Sakowicz, R., Hartman, J., and Moores, C.A. (2010). Insight into the
1336 molecular mechanism of the multitasking kinesin-8 motor. EMBO J *29*, 3437-
1337 3447.

1338 Reubold, T.F., Eschenburg, S., Becker, A., Kull, F.J., and Manstein, D.J.
1339 (2003). A structural model for actin-induced nucleotide release in myosin. Nat
1340 Struct Biol *10*, 826-830.

1341 Rice, S., Cui, Y., Sindelar, C., Naber, N., Matuska, M., Vale, R., and Cooke,
1342 R. (2003). Thermodynamic properties of the kinesin neck-region docking to
1343 the catalytic core. Biophys J *84*, 1844-1854.

1344 Rice, S., Lin, A.W., Safer, D., Hart, C.L., Naber, N., Carragher, B.O., Cain,
1345 S.M., Pechatnikova, E., Wilson-Kubalek, E.M., Whittaker, M.*, et al.* (1999). A
1346 structural change in the kinesin motor protein that drives motility. Nature *402*,
1347 778-784.

1348 Sablin, E.P., Kull, F.J., Cooke, R., Vale, R.D., and Fletterick, R.J. (1996).
1349 Crystal structure of the motor domain of the kinesin-related motor ncd. Nature
1350 *380*, 555-559.

1351 Sali, A., and Blundell, T.L. (1993). Comparative protein modelling by
1352 satisfaction of spatial restraints. J Mol Biol *234*, 779-815.

1353 Scarabelli, G., and Grant, B.J. (2013). Mapping the structural and dynamical
1354 features of kinesin motor domains. PLoS Comput Biol *9*, e1003329.

1355 Schnitzer, M.J., Visscher, K., and Block, S.M. (2000). Force production by
1356 single kinesin motors. Nat Cell Biol *2*, 718-723.

1357 Shen, M.Y., and Sali, A. (2006). Statistical potential for assessment and
1358 prediction of protein structures. Protein Sci *15*, 2507-2524.

1359 Sindelar, C.V. (2011). A seesaw model for intermolecular gating in the kinesin
1360 motor protein. Biophys Rev *3*, 85-100.

1361 Sindelar, C.V., and Downing, K.H. (2007). The beginning of kinesin's force-
1362 generating cycle visualized at 9-A resolution. J Cell Biol *177*, 377-385.

1363 Sindelar, C.V., and Downing, K.H. (2010). An atomic-level mechanism for
1364 activation of the kinesin molecular motors. Proc Natl Acad Sci U S A *107*,
1365 4111-4116.

Skiniotis, G., Surrey, T., Altmann, S., Gross, H., Song, Y.H., Mandelkow, E., and Hoenger, A. (2003). Nucleotide-induced conformations in the neck region of dimeric kinesin. EMBO J *22*, 1518-1528.

Song, H., and Endow, S.A. (1998). Decoupling of nucleotide- and microtubule-binding sites in a kinesin mutant. Nature *396*, 587-590.

Soppina, V., Norris, S.R., Dizaji, A.S., Kortus, M., Veatch, S., Peckham, M., and Verhey, K.J. (2014). Dimerization of mammalian kinesin-3 motors results in superprocessive motion. Proc Natl Acad Sci U S A *111*, 5562-5567.

Soppina, V., and Verhey, K.J. (2014). The family-specific K-loop influences the microtubule on-rate but not the superprocessivity of kinesin-3 motors. Mol Biol Cell.

Sosa, H., Dias, D.P., Hoenger, A., Whittaker, M., Wilson-Kubalek, E., Sablin, E., Fletterick, R.J., Vale, R.D., and Milligan, R.A. (1997). A model for the microtubule-Ncd motor protein complex obtained by cryo-electron microscopy and image analysis. Cell *90*, 217-224.

Sosa, H., and Milligan, R.A. (1996). Three-dimensional structure of ncd-decorated microtubules obtained by a back-projection method. J Mol Biol *260*, 743-755.

Sousa, D., and Grigorieff, N. (2007). Ab initio resolution measurement for single particle structures. J Struct Biol *157*, 201-210.

Stokin, G.B., and Goldstein, L.S. (2006). Linking molecular motors to Alzheimer's disease. J Physiol Paris *99*, 193-200.

Svoboda, K., Schmidt, C.F., Schnapp, B.J., and Block, S.M. (1993). Direct observation of kinesin stepping by optical trapping interferometry. Nature *365*, 721-727.

Tomishige, M., and Vale, R.D. (2000). Controlling kinesin by reversible disulfide cross-linking. Identifying the motility-producing conformational change. J Cell Biol *151*, 1081-1092.

Topf, M., Lasker, K., Webb, B., Wolfson, H., Chiu, W., and Sali, A. (2008). Protein structure fitting and refinement guided by cryo-EM density. Structure *16*, 295-307.

Uchimura, S., Oguchi, Y., Hachikubo, Y., Ishiwata, S., and Muto, E. (2010). Key residues on microtubule responsible for activation of kinesin ATPase. EMBO J *29*, 1167-1175.

Vale, R.D. (1996). Switches, latches, and amplifiers: common themes of G proteins and molecular motors. J Cell Biol *135*, 291-302.

Vale, R.D. (2003). The molecular motor toolbox for intracellular transport. Cell *112*, 467-480.

Vale, R.D., and Milligan, R.A. (2000). The way things move: looking under the hood of molecular motor proteins. Science *288*, 88-95.

Varga, V., Helenius, J., Tanaka, K., Hyman, A.A., Tanaka, T.U., and Howard, J. (2006). Yeast kinesin-8 depolymerizes microtubules in a length-dependent manner. Nat Cell Biol *8*, 957-962.

Visscher, K., Schnitzer, M.J., and Block, S.M. (1999). Single kinesin molecules studied with a molecular force clamp. Nature *400*, 184-189.

Woehlke, G., Ruby, A.K., Hart, C.L., Ly, B., Hom-Booher, N., and Vale, R.D. (1997). Microtubule interaction site of the kinesin motor. Cell *90*, 207-216.

Yun, M., Zhang, X., Park, C.G., Park, H.W., and Endow, S.A. (2001). A structural pathway for activation of the kinesin motor ATPase. EMBO J *20*, 2611-2618.

Figure 1

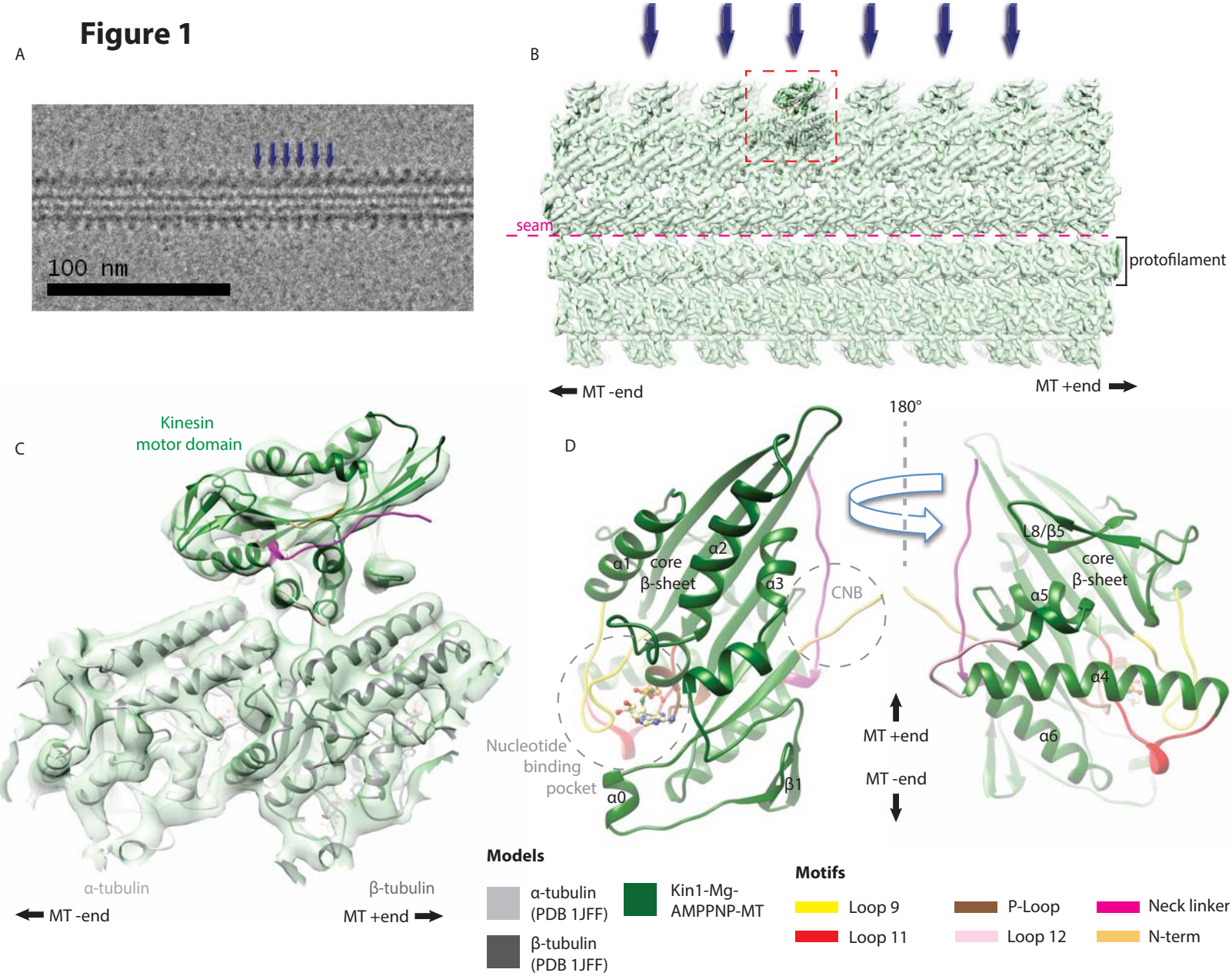
A
100 nm
B
seam
protofilament
MT -end
MT +end
C
Kinesin
motor domain
α-tubulin
β-tubulin
MT -end
MT +end
D
180°
α1
core
β-sheet
α2
α3
CNB
Nucleotide
binding
pocket
α0
β1
L8/β5
core
β-sheet
α5
α4
α6
MT +end
MT -end
Models
α-tubulin
(PDB 1JFF)
β-tubulin
(PDB 1JFF)
Kin1-Mg-
AMPPNP-MT
Motifs
Loop 9
Loop 11
P-Loop
Loop 12
Neck linker
N-term

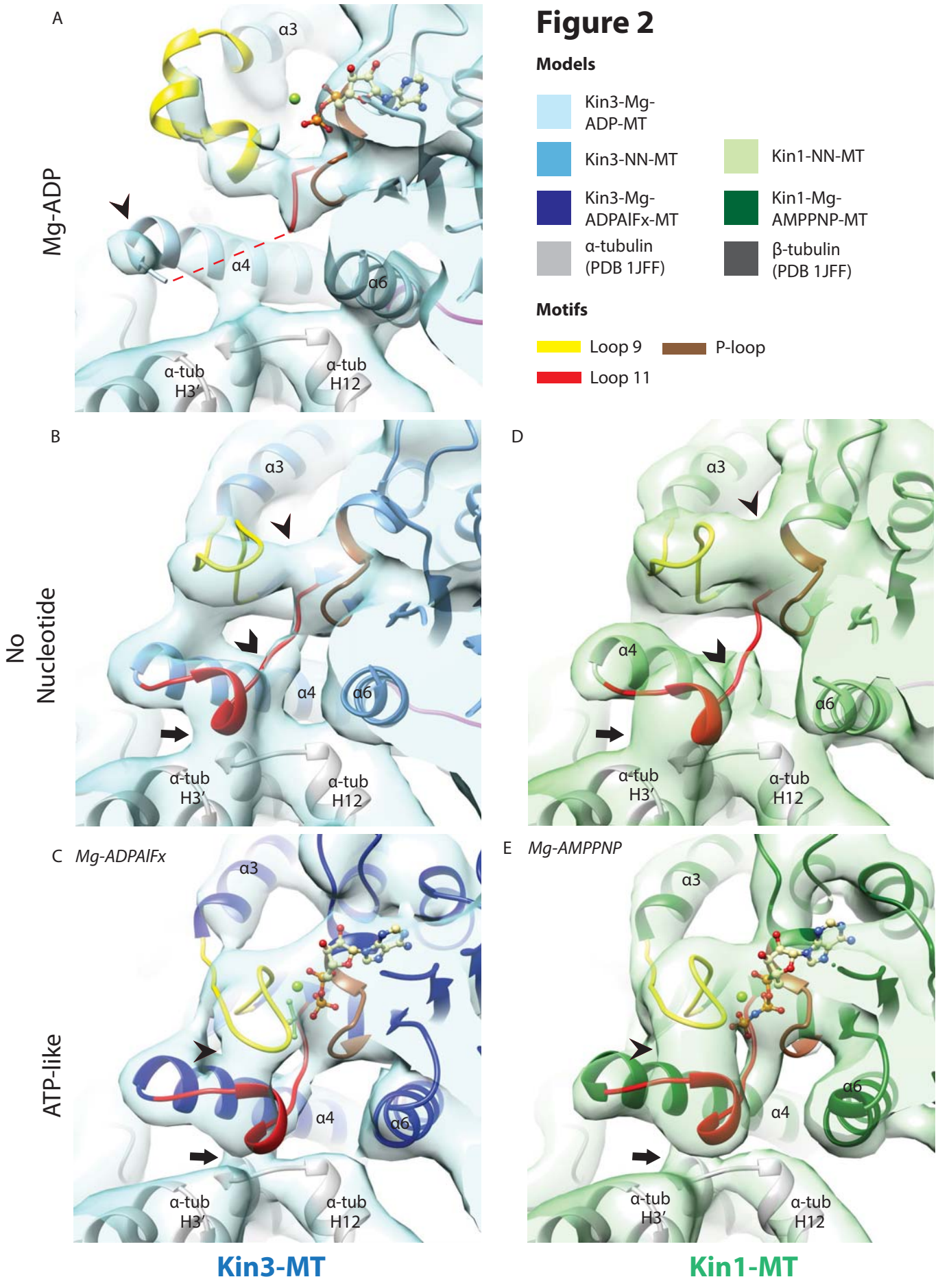
Figure 2
Models
Kin3-Mg-ADP-MT
Kin3-NN-MT
Kin3-Mg-ADPAlFx-MT
α-tubulin (PDB 1JFF)
Kin1-NN-MT
Kin1-Mg-AMPPNP-MT
β-tubulin (PDB 1JFF)
Motifs
Loop 9
P-loop
Loop 11
A
Mg-ADP
B
No Nucleotide
C
Mg-ADPAlFx
ATP-like
D
E
Mg-AMPPNP
α3
α4
α6
α-tub H3′
α-tub H12
Kin3-MT
Kin1-MT

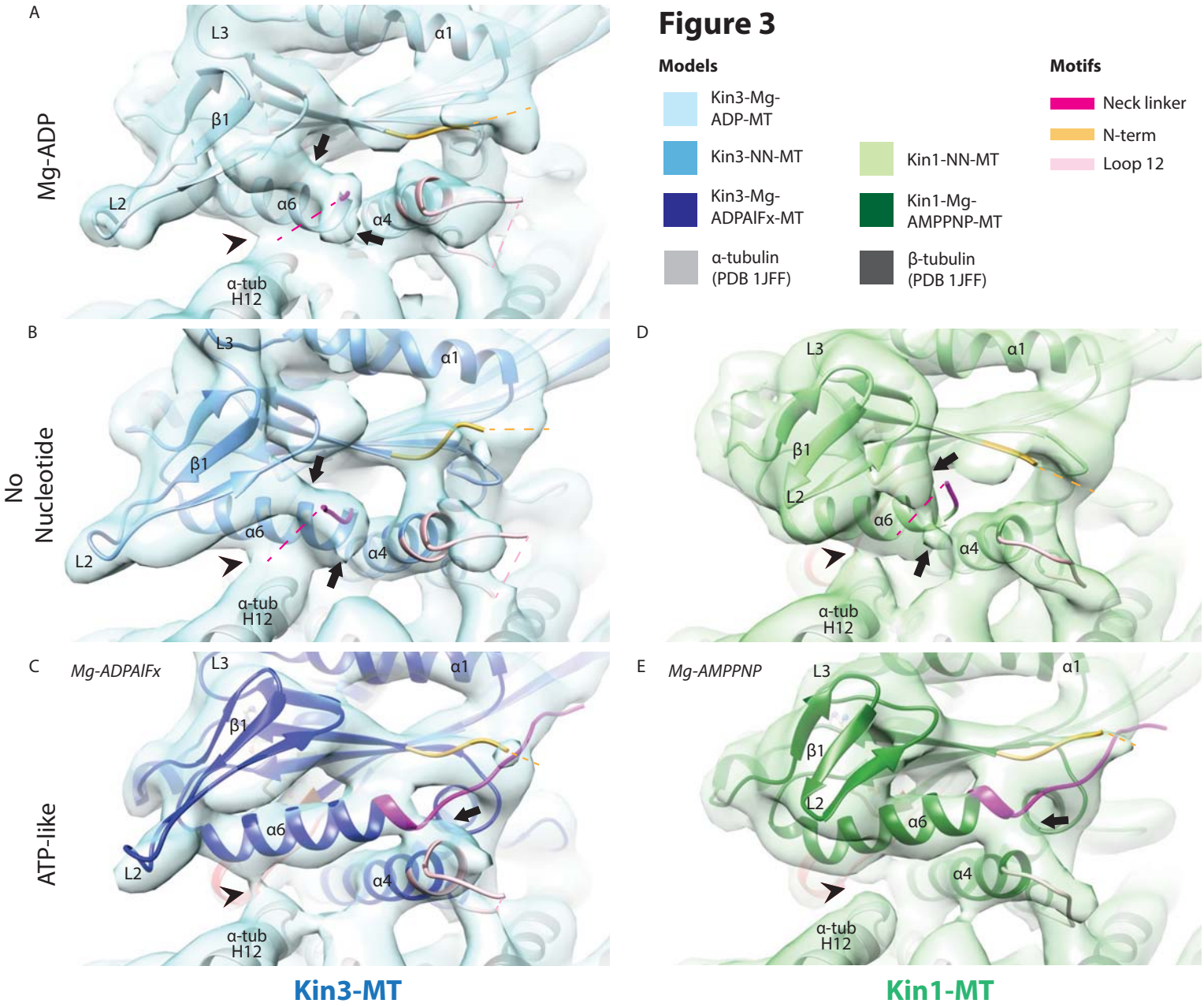
A
Mg-ADP
L3
α1
β1
L2
α6
α4
α-tub
H12
B
No
Nucleotide
L3
α1
β1
α6
L2
α4
α-tub
H12
C
Mg-ADPAlFx
ATP-like
L3
α1
β1
α6
L2
α4
α-tub
H12
D
L3
α1
β1
L2
α6
α4
α-tub
H12
E
Mg-AMPPNP
L3
α1
β1
L2
α6
α4
α-tub
H12
Figure 3
Models
Kin3-Mg-ADP-MT
Kin3-NN-MT
Kin3-Mg-ADPAlFx-MT
α-tubulin (PDB 1JFF)
Kin1-NN-MT
Kin1-Mg-AMPPNP-MT
β-tubulin (PDB 1JFF)
Motifs
Neck linker
N-term
Loop 12
Kin3-MT
Kin1-MT

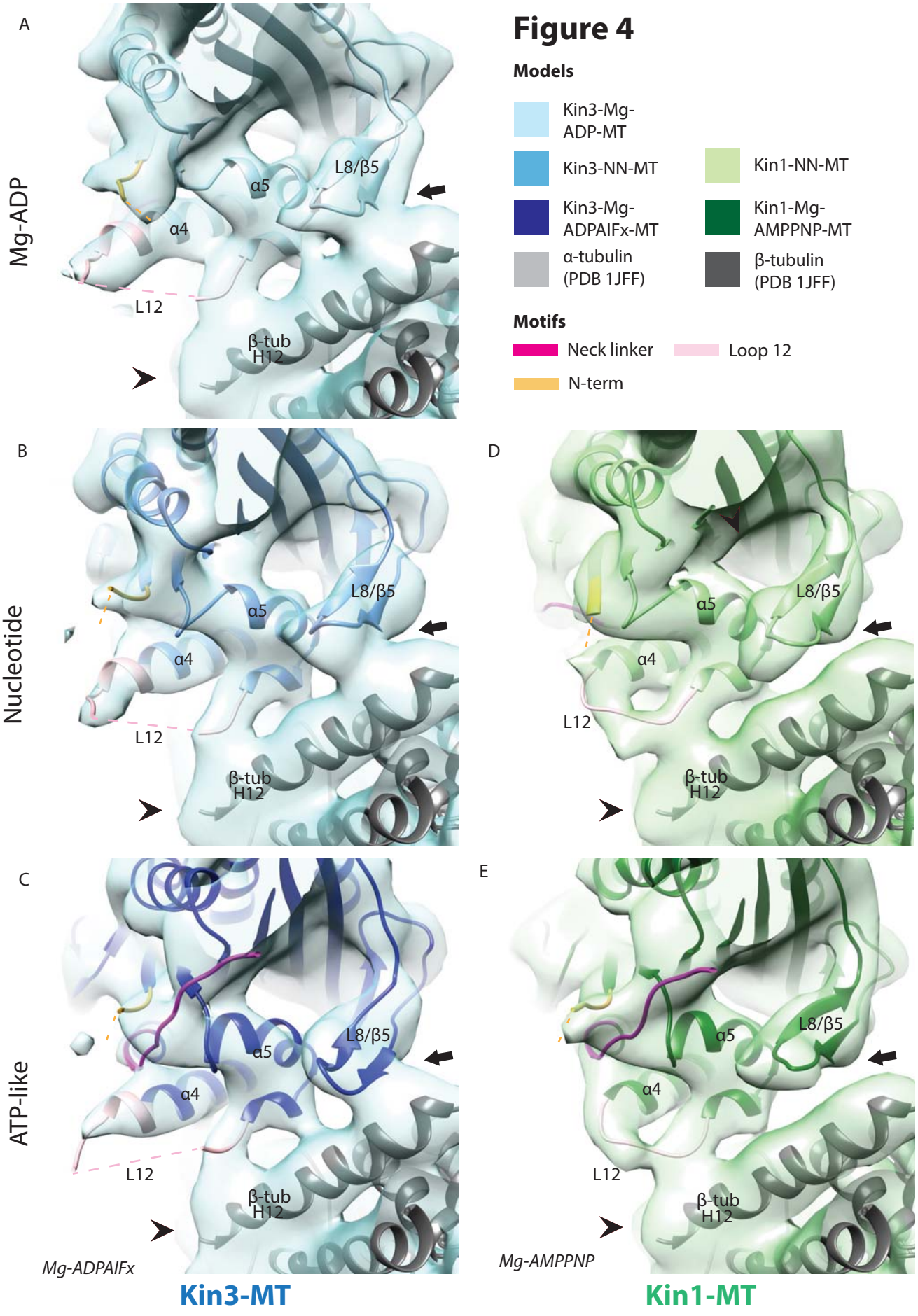
A
Mg-ADP
α5
L8/β5
α4
L12
β-tub
H12
B
No
Nucleotide
α5
L8/β5
α4
L12
β-tub
H12
C
ATP-like
α5
L8/β5
α4
L12
β-tub
H12
Mg-ADPAlFx
Kin3-MT
D
α5
L8/β5
α4
L12
β-tub
H12
E
α5
L8/β5
α4
L12
β-tub
H12
Mg-AMPPNP
Kin1-MT
Figure 4
Models
Kin3-Mg-ADP-MT
Kin3-NN-MT
Kin3-Mg-ADPAlFx-MT
α-tubulin (PDB 1JFF)
Kin1-NN-MT
Kin1-Mg-AMPPNP-MT
β-tubulin (PDB 1JFF)
Motifs
Neck linker
Loop 12
N-term

Figure 5

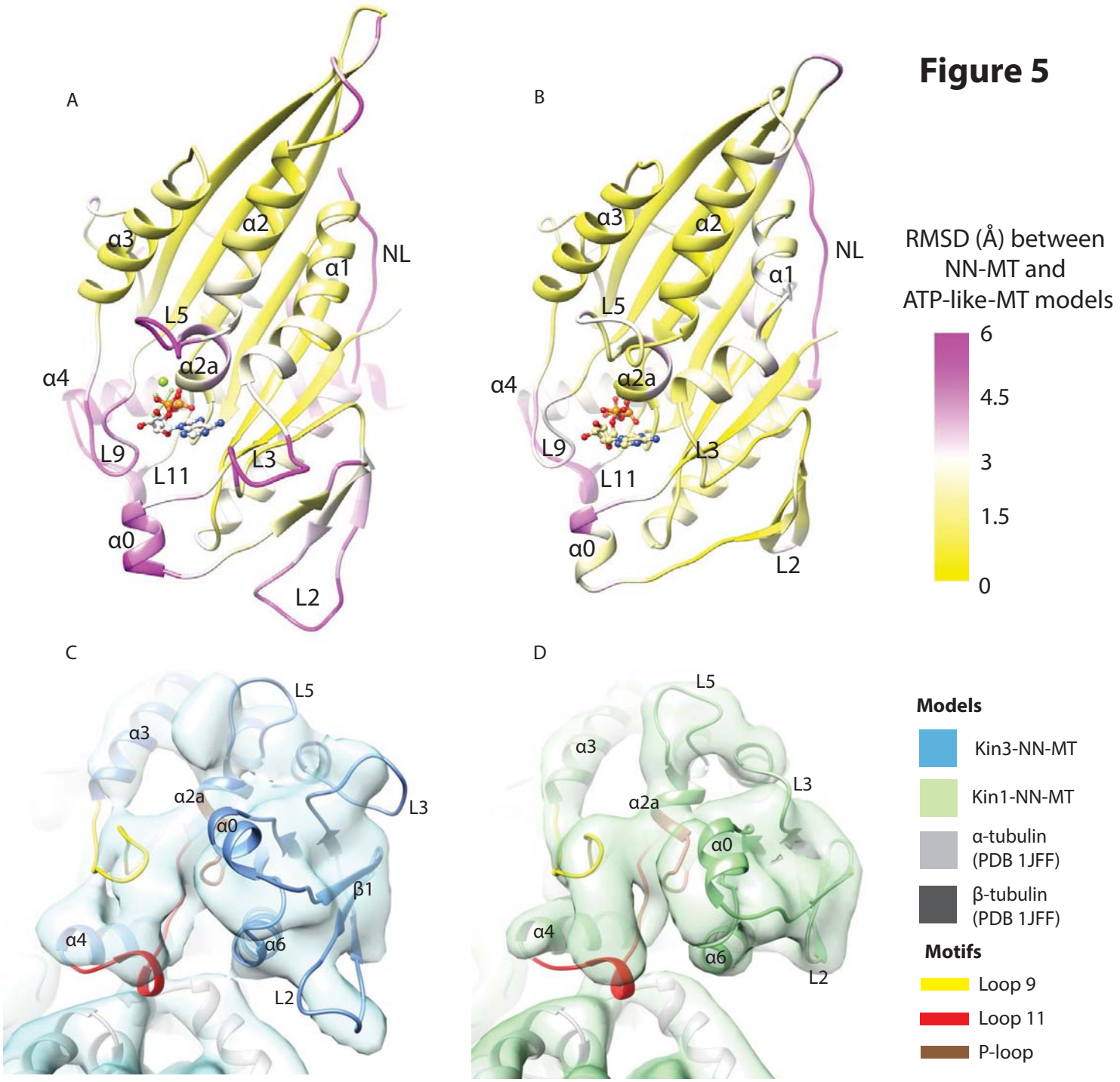
A
α3
α2
NL
α1
L5
α2a
α4
L9
L11
L3
α0
L2
B
α3
α2
NL
α1
L5
α4
α2a
L9
L3
L11
α0
L2
RMSD (Å) between NN-MT and ATP-like-MT models
6
4.5
3
1.5
0
C
L5
α3
α2a
L3
α0
β1
α4
α6
L2
D
L5
α3
L3
α2a
α0
α4
α6
L2
Models
Kin3-NN-MT
Kin1-NN-MT
α-tubulin (PDB 1JFF)
β-tubulin (PDB 1JFF)
Motifs
Loop 9
Loop 11
P-loop

Figure 6

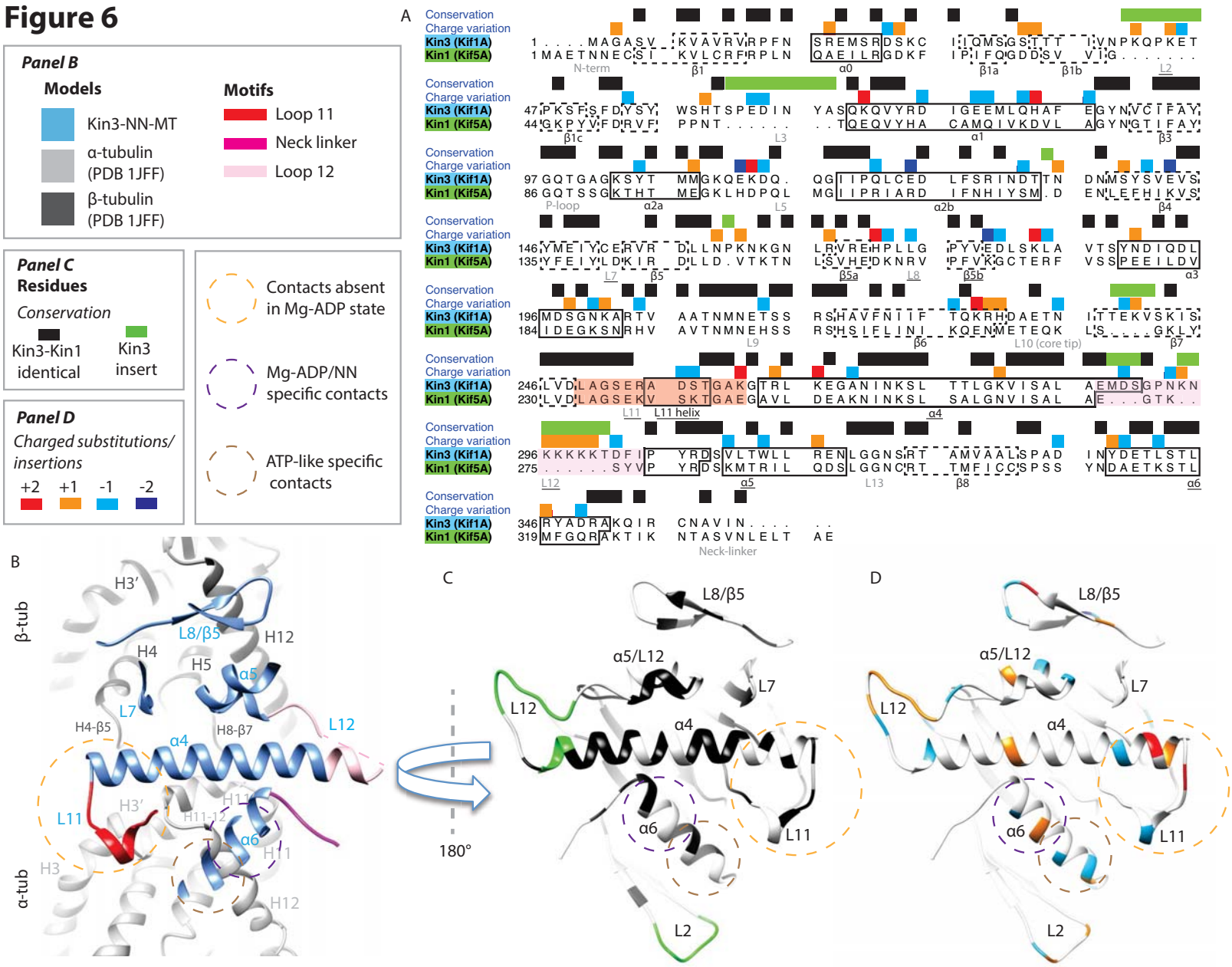
Panel B
Models
Kin3-NN-MT
α-tubulin (PDB 1JFF)
β-tubulin (PDB 1JFF)
Motifs
Loop 11
Neck linker
Loop 12
Panel C
Residues
Conservation
Kin3-Kin1 identical
Kin3 insert
Contacts absent in Mg-ADP state
Mg-ADP/NN specific contacts
ATP-like specific contacts
Panel D
Charged substitutions/ insertions
+2 +1 -1 -2
A
Conservation
Charge variation
Kin3 (Kif1A)
Kin1 (Kif5A)
N-term
β1
α0
β1a
β1b
L2
β1c
L3
α1
β3
P-loop
α2a
L5
α2b
β4
L7
β5
β5a
L8
β5b
α3
L9
β6
L10 (core tip)
β7
L11
L11 helix
α4
L12
α5
L13
β8
α6
Neck-linker
B
β-tub
α-tub
H3′
L8/β5
H12
H4
H5
α5
L7
H4-β5
H8-β7
L12
α4
L11
H3′
H11
H11-12
α6
H11
H3
H12
180°
C
L8/β5
α5/L12
L7
L12
α4
α6
L11
L2
D
L8/β5
α5/L12
L7
L12
α4
α6
L11
L2

Figure 7

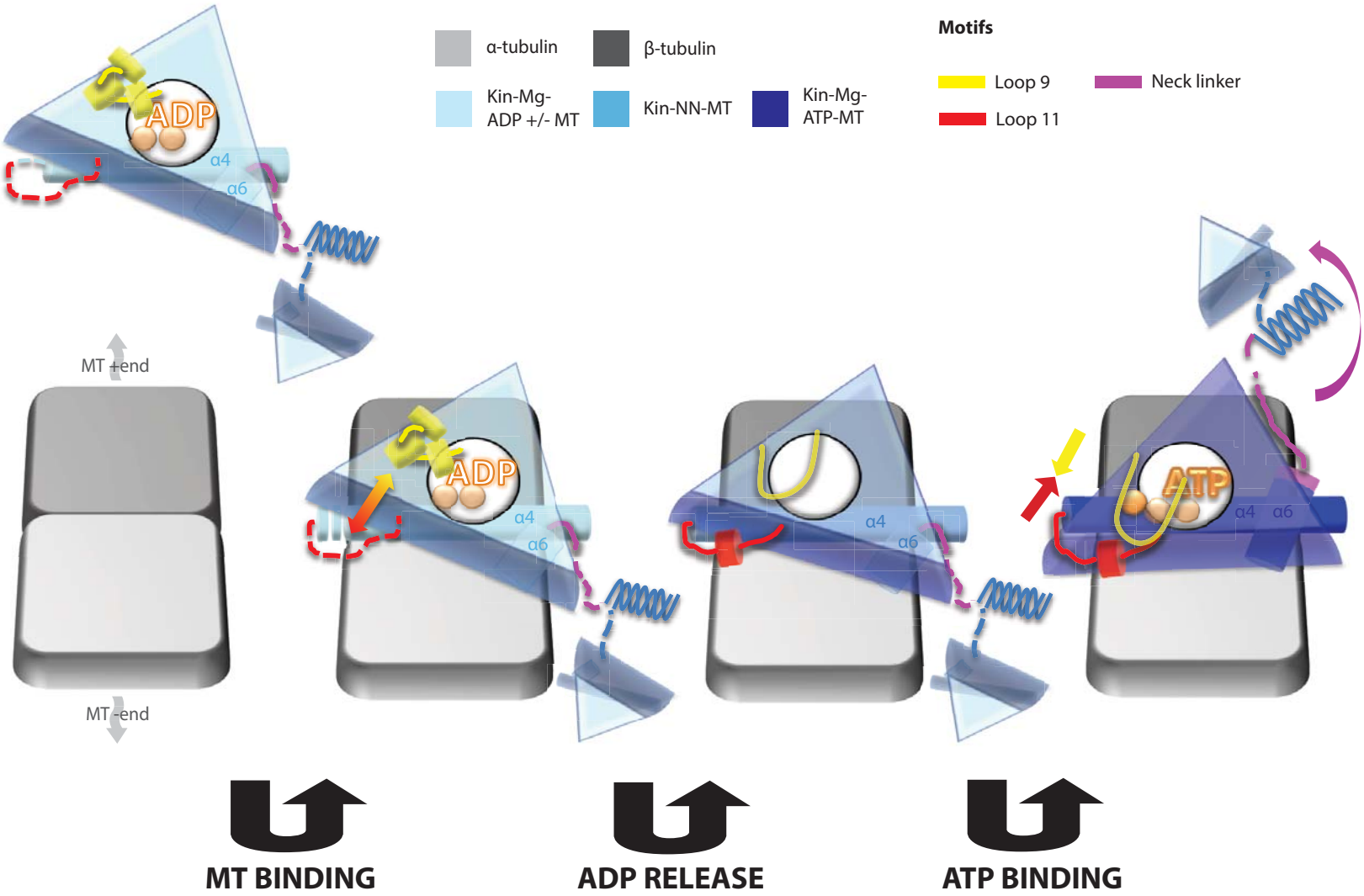
α-tubulin
β-tubulin
Kin-Mg-
ADP +/- MT
Kin-NN-MT
Kin-Mg-
ATP-MT
Motifs
Loop 9
Neck linker
Loop 11
ADP
α4
α6
MT +end
MT -end
ADP
α4
α6
α4
α6
ATP
α4
α6
MT BINDING
ADP RELEASE
ATP BINDING